(12) INTERNATIONAL APPLICATION PUBLISHED UNDER THE PATENT COOPERATION TREATY (PCT)

(19) World Intellectual Property Organization
International Bureau

(43) International Publication Date
15 November 2018 (15.11.2018)

WIPO | PCT

(10) International Publication Number
WO 2018/209111 A1

(51) International Patent Classification:
G01N 33/551 (2006.01) *G01N 33/553* (2006.01)

(21) International Application Number:
PCT/US2018/032103

(22) International Filing Date:
10 May 2018 (10.05.2018)

(25) Filing Language: English

(26) Publication Language: English

(30) Priority Data:
62/504,307 10 May 2017 (10.05.2017) US

(71) Applicant: THE REGENTS OF THE UNIVERSITY OF CALIFORNIA [US/US]; 1111 Franklin Street, 12th Floor, Oakland, California 94607 (US).

(72) Inventors: WEISS, Shimon; 807 Westholme Ave., Los Angeles, California 90024 (US). **PARK, Kyoungwon**; Ogeum Ro 35 GIL, Hyundai APT 35-305, Songpa-gu, Seoul (KR). **KUO, Yung**; 10969 Rochester Ave., Apt. 405, Los Angeles, California 90024 (US). **CHANG, Sunny Chun**; 3120 Sawtelle Blvd., Los Angeles, California 90066 (US). **SHVADCHAK, Volodymyr**; Koulova 12, Apt. 13, 16600 Prague (CZ). **LI, Jianqing**; 1844 Midvale Ave., Apt.10, Los Angeles, California 90025 (US).

(74) Agent: SERAPIGLIA, Gerard B.; Gates & Cooper LLP, 6060 Center Drive, Suite 830, Los Angeles, CA 90045 (US).

(81) Designated States *(unless otherwise indicated, for every kind of national protection available)*: AE, AG, AL, AM, AO, AT, AU, AZ, BA, BB, BG, BH, BN, BR, BW, BY, BZ, CA, CH, CL, CN, CO, CR, CU, CZ, DE, DJ, DK, DM, DO, DZ, EC, EE, EG, ES, FI, GB, GD, GE, GH, GM, GT, HN, HR, HU, ID, IL, IN, IR, IS, JO, JP, KE, KG, KH, KN, KP, KR, KW, KZ, LA, LC, LK, LR, LS, LU, LY, MA, MD, ME, MG, MK, MN, MW, MX, MY, MZ, NA, NG, NI, NO, NZ, OM, PA, PE, PG, PH, PL, PT, QA, RO, RS, RU, RW, SA, SC, SD, SE, SG, SK, SL, SM, ST, SV, SY, TH, TJ, TM, TN, TR, TT, TZ, UA, UG, US, UZ, VC, VN, ZA, ZM, ZW.

(84) Designated States *(unless otherwise indicated, for every kind of regional protection available)*: ARIPO (BW, GH, GM, KE, LR, LS, MW, MZ, NA, RW, SD, SL, ST, SZ, TZ,

(54) Title: MEMBRANE INSERTION OF POTENTIAL SENSING NANORODS

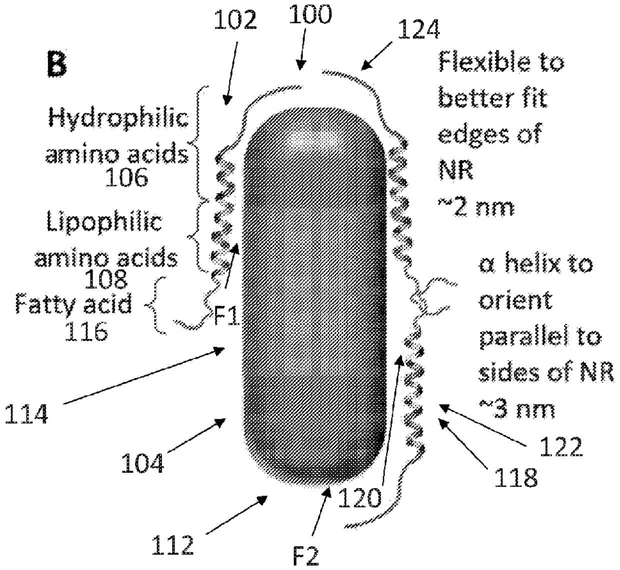

(57) Abstract: A membrane voltage nanosensor including an inorganic semiconductor nanoparticle functionalized with a rationally designed peptide. The peptide enables the nanosensor to self-insert into and through a lipid membrane and with a desired orientation (i.e., perpendicular to the membrane normal). Once inserted, the nanosensor senses a membrane potential via a Quantum Confined Stark Effect, e.g., with a single-nanoparticle sensitivity. Example systems comprising one or more of the nanosensors could be used to simultaneously record action potentials from multiple neurons in a large field-of-view over a long time duration, or to record electrical signals on the nanoscale (such as across one synapse).

[Continued on next page]

UG, ZM, ZW), Eurasian (AM, AZ, BY, KG, KZ, RU, TJ, TM), European (AL, AT, BE, BG, CH, CY, CZ, DE, DK, EE, ES, FI, FR, GB, GR, HR, HU, IE, IS, IT, LT, LU, LV, MC, MK, MT, NL, NO, PL, PT, RO, RS, SE, SI, SK, SM, TR), OAPI (BF, BJ, CF, CG, CI, CM, GA, GN, GQ, GW, KM, ML, MR, NE, SN, TD, TG).

Published:

— *with international search report (Art. 21(3))*

— *before the expiration of the time limit for amending the claims and to be republished in the event of receipt of amendments (Rule 48.2(h))*

— *with sequence listing part of description (Rule 5.2(a))*

MEMBRANE INSERTION OF POTENTIAL SENSING NANORODS

CROSS REFERENCE TO RELATED APPLICATIONS

This application claims the benefit under 35 U.S.C. Section 119(e) of co-pending and commonly-assigned U.S. Provisional Patent Application Serial No. 62/504,307, filed on May 10, 2017, by Shimon Weiss, Kyoungwon Park, Yung Kuo, Sunny Chun Chang, Volodymyr Shvadchak, and Jianqing Li, entitled "MEMBRANE INSERTION OF POTENTIAL SENSING NANORODS," client reference number 2017-710, which application is incorporated by reference herein.

SEQUENCE LISTING

The instant application contains a Sequence Listing which has been filed electronically in ASCII format and is hereby incorporated by reference in its entirety. Said ASCII copy, created on May 9, 2018, is named 30435_333-WO-U1_SL.txt and is 1056 bytes in size.

STATEMENT REGARDING FEDERALLY SPONSORED RESEARCH AND DEVELOPMENT

This invention was made with Government support under DE-FCO2-02ER63421, awarded by the U.S. Department of Energy. The Government has certain rights in the invention.

TECHNICAL FIELD

This invention relates to systems and methods for measuring membrane potential using nanoparticles.

BACKGROUND OF THE INVENTION

Recent advances in inorganic colloidal synthesis methods have afforded the construction of functional semiconductor (SC) nanoparticles (NPs) with ever-increasing control over size, shape, composition, and sophisticated heterostructures that exhibit unique photophysical, chemical and electronic properties (*1-4*). This precise command of nanoscale materials synthesis has allowed for the exquisite engineering of excited state wavefunctions (*5-7*), charge confinement, spatiotemporal control of charge-separated states (*8*), and manipulation of Fermi levels and redox potentials. As a result, SC NPs have proved to be very useful in numerous applications in optoelectronics (*9,10*), biological imaging (*11*), sensing (*12-14*), catalysis (*15*), and energy harvesting (*16*).

Integrating inorganic nanomaterials with naturally evolved or synthetically evolved biological machineries could yield highly sophisticated hybrid nanobiomaterials that outperform biological-only or inorganic-only materials (17). Such materials could be self-assembled by biomolecular recognition while maintaining the superior properties of inorganic materials (*18, 19*). Self-assembly of inorganic components by biomolecular recognition could align components in defined geometries, spatial orientations, and structures. In addition, careful design and control of the organic-inorganic interface could afford hybridization of electronic states, enhancement of radiationless energy transfer or electron transfer, or matching of Fermi levels with redox potentials.

Numerous functionalization and bioconjugation methods have been developed for the integration of inorganic-biological hybrid nanomaterials that are water soluble and biologically active (*20, 21*). Such hybrid nanomaterials have been used for *in vitro* biosensing, intra-cellular biological imaging (*22*), single protein tracking in live cells (*20*), and *in vivo* molecular imaging with favorable *in vivo* biodistribution and targeting properties (including renal clearance) (*11, 23, 24*).

Much fewer attempts have been made to functionalize nanomaterials in a way that will allow their integration into the membrane. The ability to impart membrane protein-like properties to NPs could afford their targeting and insertion into the lipid bilayer and the construction of membrane-embedded hybrid nanomaterials with useful functions. For example, a few attempts have been made to target and insert (very small, < 3nm) SC quantum dots (QDs) into the lipid bilayer. Al-Jamal *et al.* incorporated very small QDs in between the two lipid layers of the vesicle's bilayer, proved by fluorescence microscopy (*24*). Kloepfer *et al. (26)* reported the transmission electron microscopy (TEM) micrographic evidence of QDs inserted into vesicles' membranes. Gopalakrishnan *et al. (27)* successfully delivered lipophilic QDs (that were first loaded to vesicles' membranes) into membranes of HEK293 cells *via* vesicle fusion. Wi *et al.* (28) investigated the maximum allowed QDs' size both experimentally and theoretically that could still afford membrane insertion. Recently, insertion of other types of nanomaterials into the membrane was demonstrated. Synthetic ion channels made from DNA nanostructures (*29, 30*) and ion channels made from carbon nanotubes (*31*) were successfully inserted into lipid bilayers while maintaining functional ion transport across the membrane.

Following works on asymmetric type-II (conduction band and valence band minima are spatially separated) seeded nanorods (NRs) at low temperature on the single particle level (*6, 32*) and at room temperature on the ensemble level (*33*), we recently demonstrated that these NRs exhibit a large quantum confined Stark effect (QCSE) at room temperature on the single particle level (34). Marshall et al. (35) calculated that QCSE of simple type-I QDs (conduction band and valence band minima spatially overlapped) and showed that they have high enough sensitivity to detect action potential with superior S/N ratio to the conventional voltage sensitive dyes. QCSE of asymmetric type-II NRs is predicated to exhibit even higher voltage sensitivity (38) than voltage indicators such as those in (36, 37). No attempts, to the best of our knowledge, have been made, however, to target and insert rod shaped nanoparticles into the lipid bilayer. In particular, membrane insertion of NRs with length larger than the membrane thickness (~4 nm) has not been demonstrated thus far.

SUMMARY OF THE INVENTION

To overcome the limitations described above, and to overcome other limitations that will become apparent upon reading and understanding the present specification, the present invention describes design rules and peptide sequences for fabricating amphiphilic peptide coatings that impart the nanoparticles (NPs) with membrane protein-like properties. Once coated, the NPs can be integrated or inserted into cellular membranes by self-assembly. Using specifically designed NPs, a voltage potential can be measured using the florescence changes in the membrane embedded NPs. Surprisingly and unexpectedly, the voltage changes are sensitive enough to measure the changes seen in cellular processes, even on a single particle level.

Examples of cellular processes that can be sensed include, but are not limited to, neuronal signals, action potentials, membrane potential sub-threshold events, membrane potentials of cardiomyocytes, opening and closing of ion channels, ionic currents in ion channels, and vesicle fusion and neurotransmitters release. Thus, the NPs according to embodiments of the present invention have wide ranging applicability, including as research tool for cellular voltage studies, as a diagnostic tool, or as a therapeutic device. In one bioelectronics implementation, the membrane potential data could be used to correct aberrant neuronal signals. In another example, the NPs could be used to stimulate the neurons (e.g., as a neuro-implant) by generating photo-voltaic charges. In yet another implementation, the NPs could be used to image arrhythmia and guide the ablation procedure. In yet a further implementation, the NPs could be injected into the eye and be inserted into retina cell membranes so that upon light absorption, the NPs actuate neuronal signals and thus restore vision.

Thus, the present disclosure describes a composition of matter that can be embodied in many ways including, but not limited to, the following examples.

1. A composition of matter comprising peptides attached to a semiconductor nanorod or nanoparticle, wherein the peptides each comprise a hydrophilic segment connected to a lipophilic segment, the lipophilic and hydrophilic segments comprise cysteine residues, the hydrophilic segment attaches to an end of the semiconductor nanorod, the lipophilic segment attaches to a side of the semiconductor nanorod, and the cysteine residues mediate attachment of the peptides to the semiconductor nanorod.

2. The composition of matter of embodiment 1, wherein the peptides each comprise the lipophilic segment terminated by a fatty acid.

3. The composition of matter of one or any combination of the preceding embodiments, wherein the liphophilic segment comprises an alpha-helix structure.

4. The composition of matter of one or any combination of embodiments 1-3 wherein the cysteine residues are disposed in an alpha-helix structure 118 so that a side 120 of the alpha-helix structure facing the semiconductor nanorod is cysteine rich and a side of the alpha-helix structure facing an exterior is lipophilic.

5. The composition of matter of one or any combination of embodiments 1-4, wherein the hydrophilic segment comprises a flexible unstructured domain (non-helical structure) that bends around the end of the nanorod.

6. The composition of matter of one or any combination of embodiments 1-5, wherein the peptides each comprise residues that preferentially localize at a membrane-water interface.

7. The composition of matter of any combination of embodiments 1-6, wherein each of the peptides further comprise a segment of aliphatic amino acids that prevent aggregation of the peptides in solution.

8. The composition of matter of embodiment 6, wherein the aliphatic amino acids comprise a hydroxyl-containing Thr residue and an acidic residue.

9. The composition of matter of one or any combination of embodiments 1-8, wherein a sequencethe peptide is Myristoyl- CLTCALTCMECTLKCWYKRGCRGCG-COOH (SEQ ID NO:1). However, other sequences are possible. One of ordinary skill in the art understands that protein compositions or sequences that achieve the one or more functionalities describes herein for proper membrane insertion may be used.

10. The composition of matter of one or any of combination of embodiments 1-9, wherein the peptides comprise between 2 and 20 peptide chains disposed around the nanorod,

the hydrophilic segment comprises less cysteine residues (e.g., less than 5) as compared to the lipophilic segment (e.g., more than 5), and each peptide extends over at least half the length of the nanorod.

11. The composition of matter of one or any combination of embodiments 1-10, wherein the semiconductor nanorod has a length L in a range of 5 – 50 nm and a W width in a range of 1- 10 nm.

12. The composition of matter of one or any combination any of embodiments 1-11 inserted into a cell membrane 200, wherein the semiconductor nanorod has a length L longer than a thickness T of the cell membrane.

13. The composition of matter of one or any combination of embodiments 1-12 inserted into a cell membrane 200, wherein the cell membrane is a lipid bilayer.

14. The composition of matter of one or any combination of embodiments 1-13, wherein the semiconductor nanorod 104 comprises at least one material selected from CdSe and ZnSe-CdS.

15. The composition of matter of one or any combination of embodiments 1-14, wherein the semiconductor nanoparticle or nanorod 104 comprises a semiconductor having a type II band offset.

16. The composition of matter of one or any of embodiments 1-15, wherein the semiconductor nanorod 104 has a bandgap in a range of 0.6 eV - 1.77 eV.

17. A composition of matter, comprising peptides attached to a semiconductor nanorod, wherein the peptides each comprise a helical and a flexible part binding different faces of the nanorod.

The present disclosure further describes an apparatus that can be embodimed in many ways including, but not limited to, the following.

1. An apparatus for measuring a membrane potential, comprising a camera measuring one or more changes in fluorescence emitted from one or more peptide coated nanorods inserted in a cell membrane when the nanorods are excited with electromagnetic radiation. Examples of changes in fluorescence include change in fluorescence intensity, change in fluorescence emission wavelength, and/or change in fluorescence lifetime. The one or more changes include a response to one or more membrane potentials applied to the one or more nanorods by the cell membrane, the one or more nanorods each have a long axis A substantially parallel to the cell membrane's normal, and the one or more nanorods each protrude from both sides of the cell membrane. The computer coupled to the camera filters the fluorescence so as to extract the response from noise, and determines one or more magnitudes and/or one or more waveforms of the membrane potentials from the response. For example, change in fluorescence

intensity or change in emission wavelength or change in fluorescence lifetime are an indication to, or report on, change in membrane potential.

2. The apparatus for measuring the membrane potential of embodiment 1, wherein the camera measures the fluorescence comprising a wavelength shift in response to the membrane potentials, and the computer determines the one or more magnitudes and/or one or more waveforms by modeling the wavelength shift as a Quantum Confined Stark Effect.

3. The apparatus of one or any combination of embodiments 1-2, further comprising the source of the electromagnetic radiation comprising blue and/or ultraviolet (UV) electromagnetic radiation (a wavelength in a range of 350 nm – 1 micron). The nanorods emit the fluorescence in response to being excited with the electromagnetic radiation when the membrane potentials are being applied to the nanorods.

4. The apparatus of one or any of combination of embodiments 1-3, wherein the camera measures the fluorescence with an acquisition rate of more than 1 Hz -5 kHz.

5. The apparatus of one or any combination of embodiments 1-4, wherein the camera comprises an electronic imaging sensor detecting the fluorescence.

6. The apparatus of one or any combination of embodiments 1-5, wherein the computer determines the one or more magnitudes and/or waveforms of the membrane potentials from the fluorescence emitted from a single nanorod.

7. The apparatus of one or any combination of embodiments 1-6, wherein the nanorods comprise the composition of matter 100 of one or any combination of embodiments 1-17 of the composition of matter described above.

Other objects, features and advantages of the present invention will become apparent to those skilled in the art from the following detailed description. It is to be understood, however, that the detailed description and specific examples, while indicating some embodiments of the present invention, are given by way of illustration and not limitation. Many changes and modifications within the scope of the present invention may be made without departing from the spirit thereof, and the invention includes all such modifications.

BRIEF DESCRIPTION OF THE DRAWINGS

Referring now to the drawings in which like reference numbers represent corresponding parts throughout:

Fig. 1 illustrates surface functionalization. (A) A cartoon describing design principles for rendering NRs membrane protein-like. Such functionalization will favor their stable, spontaneous, insertion into the membrane with the correct vertical orientation. (B) Peptide design for implementing (A). (C) Top view of a NR coated with peptides. Red and orange colors depict Cys-rich and lipophilic faces of the α-helical peptide respectively. (D) Sequence of the designed peptide. C14-CO- stands for myristoyl acid residue attached to the N-terminal amino group. (E) A wheel diagram corresponding to the α-helical part of the peptide. Color coding is the same as in (C).

Fig. 2. Illustrates NRs interaction with membrane. (A) CryoEM micrographs of pcNRs inserted into SUVs. Scale bars are 30 nm. (B) Schematics of possible pcNRs association with lipid bilayer: (a) properly inserted (b) partially inserted (c) attached at an angle (d) horizontally embedded. (C) Histogram of insertion geometries (a) – (d). (D) Schematic of the nanorod of hydrophobic length L with two hydrophilic ends of length b and radius a. The total length of the rod is then $L + 2b$. It is shown in a piece of membrane of thickness t. The green circles show the ends of the hydrophobic rod. The

red circle denotes the center of the nanostructure, while the purple curve shows the intersection of the rod with the mid-plane of membrane. (E) Model calculations (see Supplementary SI-5) of canting angles (q) probability distribution for a membrane-inserted NR. Calculations for no hydrophobic mismatch (L = t = 4nm, blue) and for significant hydrophobic mismatch (L = 6nm, t = 4 nm, red) are shown. In both cases the rods are terminated at both ends by hydrophilic cylinders of length 2 nm (details of the model are discussed in Supplementary SI-5).

Fig. 3 illustrates delivery of pcNRs to HEK293 cells (A) Fluorescence of NRs loaded GUVs. (B) Bright field and (C) fluorescence images of pcNRs loaded GUV fused with the cell membrane. (D) Fluorescence image of HEK293 cells stained with ANEPPS (control). (E, F) pcNRs targeted to membranes at high (E) and low (F) concentrations. Scale bars are 10 μm.

Fig. 4 illustrates membrane voltage sensing of spiking HEK293 cells with pcNRs. Fluorescence images of cells stained with (A) ANEPPS and (B) pcNRs. (C) A spatially high-pass filtered image of image (B), used to highlight signals from individual pcNRs and remove background signals. Temporal band-pass filtered *ΔF/F* time trace of (D, top) ANEPPS and (F, top) pcNRs. (D, Bottom) and (F, Bottom) Each trace shares the same color as the marked open-circles in (A) or (C) respectively (see SI-7). (E, G) Overlaid *ΔF/F's* of 7 frames around the grey dash lines in (D) and (F). (D) and (F) have 23 and 19 thin lines in each sub-plots respectively. Mean traces are shown with thicker linewidth. The left most subplots with black lines are *ΔF/F* of ensemble average (generated from top panels in (D) and (F)). (Scale bars are 10 μm and the integration time is 30ms.)

Fig. 5 illustrates voltage response of pcNRs. (A) Intensity trace of a single pcNR with time-intervals of large ΔF/F modulation response ("bursts") marked with a shaded area. A frame rate of 400 Hz was used. (B) Zoom-in of intensity trace during a burst in (A); each marker represents a 2-frame average intensity during the voltage-on (*green* *squares*) and voltage-off (*red dots*) semi-period. (C) Histogram of the modulation responses for each burst, aggregating bursts from many pcNRs in a video. The first group (*red*) represents the set of patched pcNRs that exhibit the highest signal. The other three distributions represent control groups for the set of unpatched pcNRs and/or for out-of-phase modulation response.

Fig. 6 illustrates orientation-dependent absorption anisotropy of pcNRs in giant vesicle (GV) membranes. Fig. 6(A, C) are fluorescence images of pcNR-loaded vesicles. Fluorescence trajectories for NR1 (B) and NR2 (D) are marked with red arrows in (A) and (C). During the measurement, the half-wave plate was removed, leading to excitation polarization change from vertical (*F//*) to horizontal (*F*⊥). The scale bar is 20 μm and the integration time is 32 ms.

Fig. 7. Circular dichroism spectrum of designed peptides dissolved in octanol.

Fig. 8. (A~I) Confocal cross-sections of an HEK293 cell fused with pcNR-loaded vesicles. Scale bar 10 micrometers. z- step is 0.5um. (J) A birth field image of (c) for clarifying the liposomes.

Fig. 9. CryoEM images of vesicles after incubation with pcNRs. No NRs were observed to insert into the membrane. Scale bar 100nm.

Fig. 10. Image processing of voltage recording with ANEPPS. (A) Fluorescence image of ANEPPS stained spiking HEK293 cells (B) The binary image of (A) after thresholding. (C) Intensity time trace of white pixel's average in (B). (D) Blue: FFT of intensity time trace in (C). Green: The Butterworth temporal HPF function. Red: The filtered signal (frequency domain). Scale bar 10 micrometers.

Fig. 11. Image processing of voltage recording with pcNR. (A) A Butterworth type spatial HPF (B) The spatial HPF function at $\omega = 0$. (C) The binary image of Fig. 4B after thresholding. (D) Intensity time trace of white pixel's average in (C). (E) Blue: FFT of intensity time trace in (D). Green: The temporal BPF function. Red: The BPF filtered

signal. Scale bar 10 micrometers.

Fig. 12. Mean of $\{\Delta Fi/F\}$ for the two sets of patched (left) and unpatched (right) particles. The patched particles #0, #1, #3, #4, and #8 (black marks) exhibit higher absolute in-phase signal than out-of-phase and unpatched particles.

Fig. 13. Image processing of voltage recording with pcNRs. (A) Distribution of signal aggregated from patched (only particles 1, 4 and 8) and unpatched particles, computed either in-phase or out-of-phase. The red arrow highlights the negative tail of the distribution that is more pronounced for the patched set with in-phase signal. (B) Mean signal $\{\Delta F_i/F\}$ aggregated from patched (only particles 1, 4 and 8) and unpatched particles, computed either in-phase or out-of-phase. The error bars correspond to the ±1σ range. Assuming a Gaussian distribution, σ is computed as $\sigma = \mathrm{std.dev.}(\{\frac{\Delta F_i}{F}\})/\sqrt{N}$, where N is the number of elements in $\{\Delta F_i/F\}$.

Fig. 14. Canting angle distribution of NR. (A) Schematic of the nanorod in a membrane. hydrophobic length L with two hydrophilic ends of length b and radius a. The total length of the rod is then L + 2b. It is shown in a piece of membrane of thickness t. The green circles show the ends of the hydrophobic rod. The red circle denotes the center of the nanostructure, while the purple curve shows the intersection of the rod with the midplane of membrane. (B) Energy of the nanorod of radius a = 2 nm as a function of its orientation in the membrane, parameterized by , θ, h. The hydrophobic length of the rod is L = 8 nm, with hydrophilic end cylinders of length 2 nm. The energies (in units of k_BT/nm^2) are $\gamma_c^{w} = 2.0, \gamma_c^{o} = 0.1, \gamma_o^{w} = 0.1, \gamma_o^{o} = 1.0$. (C) Probability distribution for canting angle θ of a nanorod in the membrane for no hydrophobic mismatch L = t = 4 nm (blue) and significant hydrophobic mismatch L = 6 nm for the same membrane thickness. In both cases the rods are terminated at both ends by hydrophilic cylinders of length 2 nm.

Fig. 15 is a flowchart illustrating a method of making a composition of matter according to one or more embodiments of the present invention.

Fig. 16 is a flowchart illustrating a method of making an apparatus according to one or more embodiments of the present invention.

Fig. 17 illustrates an apparatus according to embodiments described herein.

Fig. 18 is a flowchart illustrating a method of measuring according to one or more embodiments of the present invention.

DETAILED DESCRIPTION OF THE INVENTION

In the detailed description of the invention, references may be made to the accompanying drawings which form a part hereof, and in which is shown by way of illustration specific embodiments in which the invention may be practiced. It is to be understood that other embodiments may be utilized and structural changes may be made without departing from the scope of the present invention. A number of different publications are also referenced herein as indicated throughout the specification. A list of these different publications can be found below in the section entitled "REFERENCES". All publications, patents, and patent applications cited herein are hereby incorporated by reference in their entirety for all purposes.

Unless otherwise defined, all terms of art, notations and other scientific terms or terminology used herein are intended to have the meanings commonly understood by those of skill in the art to which this invention pertains. In some cases, terms with commonly understood meanings are defined herein for clarity and/or for ready reference, and the inclusion of such definitions herein should not necessarily be construed to represent a substantial difference over what is generally understood in the art. Many of the techniques and procedures described or referenced herein are generally well understood and commonly employed using conventional methodology by those skilled in the art. As appropriate, procedures involving the use of commercially available kits and reagents are generally carried out in accordance with manufacturer defined protocols and/or parameters unless otherwise noted.

1. Example peptide coated NPs

NRs strongly change their optical properties (absorption and emission) when in an applied electric field that is oriented along their long axis. Thus, one optimal strategy for implementing the NRs as a detector for a transmembrane potential is to insert the NRs perpendicularly to the membrane surface, as illustrated in Fig. 1A.

The present disclosure reports on the discovery that selective insertion of cylindrical NRs into membranes in a perpendicular orientation requires different coatings on different regions of the cylindrical NRs: a lipophilic coating on cylindrical sides of the NRs and a hydrophilic coating on the tops of the NRs. Illustrative embodiments of the present invention utilize different facets and surface curvatures of the NRs to make such a non-homogeneous coating, wherein tops of the NRs that should bear a more hydrophilic coating have higher curvature than the cylindrical sides. The inventors' previously developed peptide coating technique (for solubilizing QDs in hydrophilic environments (*11, 39-43*)) utilized flexible peptides and provides good uniform coating.

Fig. 1B illustrates a peptide design for facet selective coating and consisting of a hydrophobic rigid helical domain and more flexible hydrophilic domain. Specifically, Fig. 1B illustrates a composition of matter 100, comprising peptides 102 attached to a semiconductor nanorod 104, wherein the peptides 100 each comprise a hydrophilic segment 106 connected to a lipophilic segment 108, the segments comprising cysteine residues 110, the hydrophilic segment 106 attaches to an end 112 of the semiconductor nanorod 104, the lipophilic segment 108 attaches to a side 114 of the semiconductor nanorod, and the cysteine residues 110 mediate attachment of the peptides 100 to the semiconductor nanorod 104. The lipophilic segment 108 is terminated by a fatty acid 116.

The liphophilic segment 108 comprises an alpha-helix structure 118. The cysteine residues 110 are disposed in the alpha-helix structure 118 so that a side 120 of the alpha-helix structure facing the semiconductor nanorod 104 is cysteine rich and a side 122 of the alpha-helix structure 118 facing an exterior is lipophilic.

The hydrophilic segment 106 comprises a flexible unstructured domain 124 (non-helical structure) that bends around the end 112 of the nanorod 104.

The peptides each comprise residues 126 that preferentially localize at a membrane-water interface.

Preferential binding of the rigid helical domain to sides of the NR cylinder leads to a significant difference in the lipophilicity between the sides and tops of the NR, which is necessary for perpendicular insertion into the membranes. The sequence of this prototype peptide was Myristoyl-CLTCALTCMECTLKCWYKRGCRGCG-COOH (SEQ ID NO:1), where the KRGCRGCG (SEQ ID NO:2) part served as hydrophilic flexible segment and other amino acids form a ~2.5 nm long helix that is able to cover half of the NR cylinder side (Fig. 1). Assessment using simple geometrical considerations finds that ~8-12 peptides can self-assemble in helical form on each half of a single NR (Fig. 1C) so as to cover the NR. Binding of the peptide to the NRs is mediated by 7 Cys residues: five on one face of the helical part and two in the flexible segment.

A KCWYK segment (SEQ ID NO:3) containing amino acids that preferentially localize at the membrane-water interface (*43*) was incorporated in the peptides to control the insertion depth of the peptide-covered NRs and to prevent insertion with a tilted orientation. To avoid aggregation in solution, only a short segment of aliphatic amino acids was incorporated into the peptide sequence, including three hydroxyl-containing Thr residues and one acidic residue in the hydrophobic helical segment. More details regarding the peptide design are given in methods and materials section below. The αhelicity of the peptide was confirmed by circular dichroism spectroscopy (Fig. 7) in octanol solution (dielectric constant (ε_r) = 5.1 vs membrane ≈ 5).

2. Example characterization of the NP insertion

To test peptide coated NRs' (pcNR) selective binding (perpendicular) to membranes 200, the example pcNRs 100 described above were introduced into small unilamellar vesicles (SUVs) and then imaged by EM. Quasi type-II CdSe seeded CdS rods (same recipe applied to the sample #3 in ref. (*34*)) of dimensions 4 ± 0.3 nm in diameter × 10 ± 2.2 nm in length were used for this study. The peak absorption wavelength and absorption full width half maximum (FWHM) are 604 nm and 30 nm, respectively. This seeded rod exhibits 4 nm of red shift at 400 kV/cm of electric field in air ($\varepsilon_r = 1$). The asymmetric QCSE feature indicates the asymmetric localization of CdSe seed with respect to the center of the CdS rod (*34*). This rod is selected since the chemistry is well developed which leads to the well controlled size distribution and its QCSE is confirmed at room-temperature (*34*). The pcNRs contained SUVs were then flash-frozen and imaged by cryoEM (Fig. 2A and Materials and Methods). Since cryoEM images are 2D projections, exact z-positions of pcNRs are not exactly known. For this reason, the level of insertion of pcNRs was assessed only for particles close to the vesicle's 'equator'.

The inventors analyzed over 500 pcNRs and classified them into four categories (Fig. 2B and 2C). a-type represents an ideal, symmetric and perpendicular insertion (the NR symmetrically traverses the membrane) was observed for 16.4% of all analyzed pcNRs. b-type represents partial (asymmetric) but perpendicular insertion (18% of all analyzed pcNRs). c-type represents partial, tilted insertion and is the most abundant (41.7% of all analyzed pcNRs). d-type represents horizontal insertion in between the two leaflets of the membrane (23.9% of all analyzed pcNRs). The histogram in Fig. 2C shows the partitioning in insertion geometries. If all cases of c-type insertion are ignored (since it is hard to classify parallel vs. perpendicular insertion for these cases), vertically oriented pcNRs (a- and b-type) constitute 59% of all a-, b-, and d-type insertions.

Although these percentages are only a rough estimate for the partitioning between the different insertion configurations (due to the ambiguity in z positioning) and the captured cryoEM images show only frozen snapshots of NRs' inserted into membranes, this estimate for partitioning is also reproduced in an independent fluorescence anisotropy measurement. NRs were loaded into electro-swelled giant unilamellar vesicles (GUVs) (Fig. 8). The orientation of the membrane-associated pcNRs was probed by polarization microscopy (*45*), capitalizing on the fact that NRs' absorption and emission dipoles are aligned along their long axis (*46*).

To estimate orientation of pcNRs in the membrane, the fluorescence of GUVs loaded with pcNRs was imaged using linearly polarized laser excitation. Since the absorption and emission dipoles of NRs are aligned along their long axis, polarized excitation could verify the pcNRs' orientation with respect to the cellular membrane curvature (see also Fig. 6). Analysis of the absorption dipole moment polarization anisotropy of individual pcNRs and applying a simple absorption anisotropy (AA) threshold shows that ~ 58% of the pcNRs were inserted with an orientation that is more perpendicular (*threshold* > 0) to the membrane plane, than parallel (see section 6e below). In contrast to cryoEM snapshots, AA spectroscopy and imaging on the single particle level follows NR reorientations dynamics in real time. Moreover, AA spectroscopy and imaging helps disentangle blinking dynamics from reorientation dynamics if both horizontally and vertically polarized photons are measured simultaneously. Despite testing thus far only one rationally designed α-helical peptide sequence, the data shows a sizeable fraction of pcNRs have vertical membrane orientation (~58%) and 16% of NRs were properly inserted, supporting the feasibility of the functionalization approach described herein. A control cryoEM experiment showed that as-synthesized (native ligand-coated) NRs do not insert into vesicles' membranes (Fig. 9).

The present disclosure associates fluctuations (in the polarization anisotropy measurement of the pcNRs in the vesicle) with non-rigid orientation of the pcNRs in the membrane. Furthermore, the rotational diffusion constant of the pcNRs is determined to be on the order of 10 kHz by considering a simple estimate based on the nanorod diffusing in a solvent with a viscosity of 1 kg/m·s (a thousand times the viscosity of water). This suggests that the azimuthal angle should be rotationally averaged-out on the time scale of the measurement. The observation of slower rotational fluctuations might be due to coupling to translational motion, or to fluctuation in the level of insertion (i.e. the NR moves in and out of the membrane).

In order to assess the cryoEM results, the inventors studied the equilibrium partitioning between membrane and solution of the NRs, and their orientational fluctuations within the membrane using the Boltzmann distribution and a simple model of the interaction energy of the NR with membrane and solvent (Fig. 2D and section 6I.for details). The results show that, for reasonable hydrophobic/hydrophilic energies and typical NR geometries, there is strong partitioning between the NRs and the membrane. Once embedded in the membrane, the inventors predict that rods will be canted so that their long axis does not lie along the local normal to the membrane. The mean canting angle (θ) depends on the mismatch of the length of the NR's hydrophobic region and the thickness of the membrane. From examination of the canting angle, the fluctuations of the canting angle of rods with no hydrophobic mismatch (blue curve) is estimated to be in the range of ten degrees and thus comparable to the mean. Both the mean and the fluctuations are larger for cases of large hydrophobic mismatch (red). There the mean is ~45 degrees, and the inventors expect fluctuations to significantly larger angles, based on the large tail of the angle probability distribution. This model predicts that with hydrophobic surfaces covering a length of the pcNRs comparable to the membrane thickness, the fraction of rods inserted into the membrane approaches unity in thermal equilibrium. In order to stabilize the orientation of rods in the membrane to be close to the membrane's normal, it is advantageous to include hydrophilic ends on the pcNRs tips. For reasonable lengths of these ends, they do not significantly change the partitioning of rods between the membrane and the solvent. Moreover, the model predicts a canting angle distribution (Fig. 2E) that resembles the histogram in Fig. 2C, suggesting some degree of hydrophobic mismatch (Fig. 2D). The inventors note, however, that the statistical nature of ligand exchange with the designed peptide does not necessarily impart precise hydrophobic surfaces and hydrophilic tips.

3. Example delivery method

The pcNRs described herein can be delivered to the cellular membrane by either vesicle fusion (Fig. 3A - C) or direct drop-casting method (Fig. 3E - F). Fusogenic lipids are required for vesicle fusion process. Here, we used 1,2-stearoyl-3-trimethylammonium-propane (DOTAP) or 3b-[N-(N',N'-dimethylaminoethane)-carbamoyl]cholesterol hydrochloride (DC-Chol) and a cone-shaped lipid, 1,2-dioleoyl-sn-glycero-3-phosphoethanolamine (DOPE) (27, 47, 48). Once vesicles were formed, pcNRs were loaded and their instantaneous staining could be observed (Fig. 3A). When pcNRs-loaded vesicles were added to HEK293 tissue culture, they could be delivered to cell membrane *via* fusion. Bright field image (Fig. 3B) and its corresponding fluorescence image (Fig. 3C) capture the moment of vesicle fusion. Z-stack images of the same cell are shown in Fig. 8, clearly indicating vesicle fusion and subsequent membrane staining. The pcNRs could also be added directly to the growth media of a tissue culture, as demonstrated in Fig. 3E and 3F for HEK293 cells. By diluting the concentration of pcNRs, sparse labeling could be achieved such that individual (or small aggregates of) pcNRs could be clearly observed (Fig. 3F). Interestingly, the present disclosure reports a loss in the diffraction limited fluorescence emanating from membrane inserted pcNRs within ~ 1 hour after staining, most likely due to endocytosis.

4. Example sensing techniques

The apparatus for measuring the membrane potential using the pcNRs typically comprises an imaging system measuring one or more changes in fluorescence emitted from the pcNRs inserted in a cell membrane when the nanorods are excited with electromagnetic radiation.

The one or more changes in fluorescence (e.g., change in intensity of the fluorescence and/or wavelength of the fluorescence and/or change in fluorescence lifetime) are in response to one or more membrane potentials applied to the one or more pcNRs by the cell membrane (ideally when the pcNRs each have a long axis substantially parallel to the cell membrane's normal, and the pcNRs each protrude from both sides of the cell membrane.

The imaging system typically comprises a camera such as an electronic imaging sensor (e.g., electron multiplying charge coupled device or scientific CMOS sCMOS).

In one or more embodiments, spectral shifts in the fluorescence caused by the one or more membranes are measured by splitting the fluorescence emission into 2 halves using a dichroic mirror and imaging both halves onto either 2 cameras, or 2 segments of the same camera. Individual pcNRs would show as spots in both half-images. The ratio of intensities (or other algebraic expression) for the same spot is related to the spectral shift. In one example, the splitting is performed using W-view image splitting optics providing one pair of dual wavelength images separated by a dichroic mirror onto a single camera (60).

In one or more embodiments, a computer coupled to the imaging systems filters the fluorescence so as to extract the response from noise, and determines one or more magnitudes and/or one or more waveforms of the membrane potentials from the response.

5. Example membrane voltage sensing

Membrane voltage sensing with pcNRs described herein was first tested using self-spiking HEK293 cells (*49*). This cell line exhibits self-oscillations (~3 - 4 Hz) in membrane potential once cells reach confluency (*49*). Fig. 4 shows optical recordings of these self-spiking HEK293 cells with di-8-ANEPPS (ANEPPS) (Figs. 4a, d, e, serving as positive control) and pcNRs (Figs. 4b, c, f, g). Oscillating membrane potential is resolved by ANEPPS, exhibiting ~ 10 % $\Delta F/F$ on the ensemble level (Fig. 4D top panel and section 6(i)). Bottom panel of Fig. 4D shows four $\Delta F/F$ recordings (from 4 distinct locations, averaged over 5 x 5 pixels) marked with open circles of the same color. Fig. 4A shows that these recordings are highly correlated with each other and with the ensemble average (black). These recordings were re-plotted in Fig. 4E by overlaying seven frames around every local maximum in the trajectory (guided with vertical dashed lines in Fig. 4D). The mean $\Delta F/F$ over 23 cycles are plotted with thicker lines (black: ensemble $\Delta F/F$; blue, red, green, cyan: local $\Delta F/F$'s in Fig. 4A). This result demonstrates the fidelity of membrane potential recording with ANEPPPS.

The same analysis was performed for self-spiking HEK293 cells stained with pcNRs. In contrast to the clear membrane staining of ANEPPS (Fig. 4A), pcNRs are randomly distributed in the membrane and outside of it (cloudy background). In principle, better labeling (and higher contrast images) could be achieved by multiple washes applied to the tissue culture after incubation with pcNRs (as in Fig. 3E), but multiple washes abolish self-spiking. To eliminate densely pcNRs-labeled regions and diffused background from the analysis of the data represented in Fig. 4B, a 10th order (N = 10) Butterworth type (high pass) spatial filter (HPFpixel) was applied to the image (Fig. 12A, B). The cut-off spatial frequency (ω_c) was 0.244 (pixel-1). This image processing results in improved local contrast and enables the detection/identification of single bright spots (Fig. 4C). In a subsequent step, simple thresholding (threshold = mean + 2 × standard deviation) was applied to select only bright, small pcNR-labeled regions (white pixels in Fig. 11C) for calculating the ensemble $\Delta F/F$. The spatially averaged (over all white pixels in Fig. 11C) temporal fluorescence signal is shown in Fig. 11D. Extracting membrane potential fluctuation from this signal is difficult due to photo-brightening and noise.

The inventors therefore implemented an additional temporal band pass filtering step which is a 5th order (M=5) Butterworth filter with cut-off frequencies (f_{high} = 7 Hz and f_{low} = 2.5 Hz, Fig. 11E). This process further cleans-up and highlights these oscillations by removing the slowly varying (low frequency) photo-brightening and the high frequency shot-noise (Fig. 4F, top, black line). The filtered signal in Fig. 4F (top) exhibits ~4 Hz oscillations, similar to the oscillations reported in Fig. 4D. The asymmetric voltage depolarization and repolarization signal (*48*) is not resolved here due to the long integration time (30ms). Although the ensemble $\Delta F/F$ is only ~1%, it demonstrates that pcNRs can record membrane voltage oscillation. Isolated diffraction limited white spots in Fig. 4C (representing either individual pcNRs or very small aggregates of pcNRs) were analyzed to test if pcNRs can provide single particle voltage sensitivity. Indeed, band-pass-filtered optical recordings from the individual spots marked with colored-open circles exhibit up to 5% $\Delta F/F$ voltage oscillations (Fig. 4F, cyan). Fig 4G shows (like in Fig. 4E) signal time traces of 19 consecutive cycles (7 frames per cycle). The mean value of the signal is also shown with a thicker line. Same analysis was repeated for 129 individual diffraction limited bright spots. 16 % of all cases exhibited $\Delta F/F > 1\%$.

Additional evidence for voltage sensing by pcNRs was provided by simultaneous patch clamp and fluorescence measurements. pcNRs were applied directly to wild-type HEK293 cells that were cultured on a coverslip, and fluorescence emission and membrane voltage were recorded simultaneously. Fluorescence movies were recorded in synchrony with the membrane voltage modulation (with a cycle of 2 movie frames recorded at -150 mV followed by 2 movie frames recorded at 0 mV, voltage modulation frequency of 100 Hz and recording duration of 2000 frames with 400 Hz of frame rate). Fig. 5A shows a fluorescence time trajectory recorded from a single (or possibly a small aggregate of) pcNR(s) (as judged by blinking) highlighted by an arrow in Fig. 3F. The fluorescence trajectory is highly noisy, most likely due to fluorescence intermittency (blinking) and unstable, dynamic fluctuations in membrane insertion (see discussion about membrane insertion stability in section 6(i)). A zoom-in to the trajectory at around 4.6 s (Fig. 5B) shows a zig-zag pattern in the fluorescence intensity that is synchronized with the modulated clamped voltage. For each modulation semi period, a pcNR modulation response $\Delta F/F$ was defined as the difference between voltage-on and voltage-off intensities divided by the mean time-trace intensity. The modulation response ($\Delta F/F$) exhibits a high degree of variations throughout the acquisition time (5 s) with a few spikes of high signal about 100 ms long. The inventors attribute the low reproducibility and low sensitivity of these recordings to imperfect, unstable insertion of pcNRs into the cellular membrane.

Eight (8) individual (or small clusters of) pcNRs were identified in the patched cell's membrane (or its proximity). The mean modulation response during the entire timetrace (excluding the off periods of the pcNR fluorescence blinking) was computed for each individual or small cluster. Out of 8 pcNRs, only 3 exhibited a mean absolute modulation that was higher than the mean calculated for pcNRs in membranes of non-patched cells. These 3 pcNRs, however, all have a negative mean modulation (with a $\pm 1\sigma$ error range that does not include 0), while the control group of 7 pcNRs in the membrane of non-patched cells exhibit a mean signal which is statistically indistinguishable from 0. Since the modulation response ΔF/F exhibits spikes or "bursts" of high signal that presumably correspond to brief periods of membrane insertion, we carried out an objective analysis that is focused on such brief "bursts". To reduce the effect of noise on the identification of the start and stop of burst regions we thresholded the running average of the ΔF/F modulation response. The integral modulation response in each burst i is computed as:

$$S_i = \frac{1}{F} \sum_i \Delta F_i$$

(see Example Materials and Methods section 6).

Fig. 5C shows the distribution of integral modulation responses for bursts belonging to pcNRs found in the patched cell membrane (patched in-phase, red) compared to integral modulation responses of controls that should not exhibit any correlated signal. In particular, in the out-of-phase controls, any intensity fluctuation in-phase with the voltage modulation is suppressed by averaging frames corresponding to ON and OFF voltage semi-periods (see Materials and Methods in section 6). While the controls exhibit a symmetric distribution of bursts with positive and negative values for the integral modulation response (consistent with random fluctuations), bursts of patched pcNRs show a predominance of negative integral modulation response (consistent with fluorescence reduction induced by the applied voltage). Note, however, that only 18 in-phase bursts were identified and analyzed for the 3 pcNRs associated with the patched cell membrane (and 20 out-of-phase bursts). For the non-patched cells control we identified 7 pcNRs (in non-nearest neighbor cells, to avoid possible signal leakage) yielding a total of 28 in-phase bursts (and 40 out-of-phase bursts).

6. Example materials and methods

The following methods and materials were used to obtain the data disclosed herein.

a. NR Synthesis

Quasi-Type-II NRs (CdSe seeded in CdS): Cadmium oxide (CdO, 99.99%), tri-n octylphosphine (TOP, 90%), trioctylphosphine oxide (TOPO, 99%), selenium (Se, 99.999%) and Sulfur (S, 99.5%) along with all organic solvents were purchased from Sigma-Aldrich and used without any further purification. Hexylphosphonic acid (HPA) and octadecylphosphonic (ODPA) were purchased from PCI Synthesis. A 50 ml round bottom flask was loaded with 60 mg (0.5 mmol) CdO, 280 mg ODPA and 3g TOPO. After degassing under vacuum for 1 hr at 120°C, the temperature was raised to 340°C under argon until dissolution of CdO at which point 1.8 ml TOP was injected and temperature was raised to 370°C. A solution containing 58 mg Se in 0.5 ml TOP was swiftly injected and heating mantle was removed. Final core size had a diameter of about 2.7 nm. A slight modification of previously reported methods (7) was used for seeded growth of CdS. A 50 ml round bottom flask was charged with 211 mg (1.6 mmol) CdO, 1g ODPA, 50 mg HPA and 3.46 g TOPO. The reaction flask was degassed for 3 hrs at 130°C and then temperature was raised to 340°C under argon until dissolution of CdO, at which point 1.8 ml of TOP was injected. CdSe seed solution was separated and purified for reaction by mixing with toluene and precipitating with excess methanol 3 times. Seeds were then re-dissolved in 0.6 ml TOP. The S:TOP precursor solution was prepared by mixing 51mg S (1.6mmol) in 0.6 ml TOP. The temperature was raised to 350°C for injection. The amount of dots used was 8×10^{-7} moles. The size distribution of NRs was characterized by EM, yielding 4 ± 0.3 nm for NRs' diameter and 10 ± 2.2 nm for NRs' length.

b. NR functionalization with peptides

The sequence of the two peptides used to obtain the example data disclosed herein is Myristoyl-CLTCALTCMECTLKCWYKRGCRCG-COOH (SEQ ID NO:1). Peptide was purchased from LifeTein LLC, purified to a level of 70 % by HPLC, characterized by mass spectrometry and circular dichroism (Fig. 7). The protocol for NRs functionalization with α-helical peptides is similar to the protocol reported in (*38*) with the following modifications: as-synthesized NRs were coated with hydrophobic surfactants such as TOPO or ODPA. To exchange these surfactants with the designed peptides, the surfactants were first stripped off the NRs by multiple (5~6×) methanol precipitation steps, followed by re-dissolution in pyridine 450 µl. The NR's concentration was 0.1 µM. 4.0 mg of peptides were dissolved in 50 µl of DMSO, and mixed with NRs in DMSO solution. 12µl of tetramethylammonium hydroxide (TMAOH) were added to the solution to increase the pH to 10.0 allowing the peptides to bind to the NRs' surface efficiently. The mixture was then centrifuged and redispersed in 150 µl of DMSO, in a form ready to be used for cell membrane insertion (staining).

For vesicle staining or for the cryoEM experiment, NRs in DMSO solution were eluted through a G-25Sephadex desalting column (Amersham, Piscataway, NJ) and equilibrated with PBS buffer. The pcNRs were stored at 4 °C. Assynthesized NRs emit photons of 600nm and have an initial quantum yield of 15% which was maintained after the peptide coating process.

b. Secondary structure as measured by circular dichroism

The secondary structure of the designed peptides is determined by circular dichroism (CD). The peptides were dissolved in octanol, which mimics the nonpolar interior of the cell membrane. 4 mg of the peptides were dissolved in 1 ml of octanol and the excess solid peptides were filtered out to yield a saturated peptide solution. The concentration of the saturated peptide solution was determined to be ~17 μM (~0.05 mg/ml), by the absorbance of tryptophan at 280 nm using UV-

Vis spectrometer. The CD spectrum was acquired at 25℃ under N_2 purge, using a quartz cuvette with 1 cm path length. The large, 1 cm path length was selected, due to the low solubility of the peptide in octanol and hence low absorbance of the solution when using a cuvette with 1 mm path length. The CD spectrum above 205 nm showed a characteristic alpha-helical structure, while the spectrum below 205 nm was oversaturated due to the solvent. (fig. S1).

c. Loading pcNRs into vesicles

1,2-dimyristoyl-sn-glycero-3-phosphocholine (DMPC), 1,2-dioleoyl-3-trimethylammonium propane chloride salt (DOTAP), 3b-[N-(N',N'-dimethylaminoethane)-carbamoyl] cholesterol hydrochloride (DC-Cholesterol), were purchased from Avanti Polar Lipids, Inc. Chloroform solutions of DOTAP (25 mM, 6 μl), DMPC (10 mM, 6 μl) and

DC-Cholesterol (10 mM, 6 μl) were mixed and dried in a vacuum for 4 hrs in a rotary evaporator. The film was then hydrated with 1 ml of 0.1 M sucrose containing PBS buffer with pH 6.24 overnight at 37°C in an incubator, during which time vesicles were spontaneously formed. Vesicles were stored at 4 °C unless used in experiments (they are stable and useable for about one week). For the cryoEM experiment, vesicles were extruded through a membrane with a 100 nm pore sized filter. For the fluorescence microscopy measurement, 2 µl of pcNRs (eluted through a G-25Sephadex desalting column) were added to the 10 µl of vesicle solution. pcNRs spontaneously and rapidly (~1 min) self-inserted into the vesicles' membranes. For GUVs, the same lipid composition (6 µl of 25 mM DOTAP, 6 µl of 10 mM DMPC, and 6 µl of 10 mM DC-Cholesterol) was diluted with 200 µl of chloroform. 50 µl of the lipid in chloroform solution was loaded on the indium-tin-oxide (ITO) coated glass. After drying for 30 minutes, the other ITO coated glass was placed so as to face the lipid dried on the ITO glass and so that the two glasses were separated by the 3 mm thickness of an O-ring, forming an aqueous chamber for electro-swelling. 10 Hz of 1.0 V square voltage pulse was applied to the two ITO glasses for 20 mins, followed by GUV preparation for imaging.

d. Cryo electron microscopy (cryoEM)

For the cryoEMelectron microscopy measurement, 10 µl of pcNRs (eluted through a G-25Sephadex desalting column, producing 0.05 µM) were added to 50 µl of vesicle solution (0.27 mM lipid concentration). An aliquot (3 µl) of sample was placed on a holey carbon-coated Quantifoil grid, manually blotted with filter paper, and plunged into liquid ethane to make a cryoEM grid with vesicles embedded in vitreous ice. The grid was transferred to a Gatan 626 cryo sample holder cooled down by liquid nitrogen, and inserted into an FEI TF20 cryoelectron microscope for imaging at a 200 kV operating voltage. Images were recorded at several magnifications on a 4k x 4k CCD camera (TVIPS) at ~5 µm under focus with an accumulated electron dosage of ~20 $e^-/Å^2$ on each sample area.

e. pcNR orientation measurement

To estimate pcNRs' orientation in membranes, vesicles were made and attached to the microscopy cover glass. 8 µl (25 mM in chloroform) of 1,2-stearoyl-3-trimethylammoniumpropane (DOTAP) and 1µl (25 mM in chloroform) of 1,2-dioleoyl-*sn*-glycero-3- phosphoethanolamine (DOPE) were mixed and dried under ambient condition. 100 µl of 100 mM NaCl with 1 volume percent of glycerol of distilled H_2O (dH_2O) were then added to the dried lipids, and stored in a 4°C refrigerator for 24 hrs, followed by one minute of sonication. 5 µl of the vesicle solution was then loaded to the cover glass. To immobilize the vesicles, 500 µl of 100 mM NaCl in dH_2O (no glycerol) were added to the vesicle solution. After 10 minutes, immobilized giant vesicles (GV) could be observed. Finally, pcNRs were added to the vesicle-containing water droplet. Fig. 6A and 6C show fluorescence images of pcNRs loaded vesicles, excited with vertically polarized light. 200 frame movies were acquired and time trajectories from individual pcNRs were analyzed. During the movie acquisition, the excitation polarization was rotated by 90° by removing a half-wave plate in the excitation path. pcNRs at 0°, 90°, 180°, 270° of the vesicles' cross-section (at horizontal or vertical plane) were selected and analyzed. The representative intensity trajectories from the membrane inserted pcNRs during polarization modulation are shown in Fig. 6A and 6B. From such trajectories, absorption anisotropy

$$AA = \frac{FP_{//} - FP_{\perp}}{FP_{//} + FP_{\perp}}$$

was obtained by measuring the fluorescence signal. 26 pcNRs were analyzed and 15 out of them show AA corresponding to vertical orientation in membrane (AA > 0 for pcNRs in the vertical plane of GUV) indicating a preference towards vertical insertion, consistent with cryoEM results.

	Vertical plane	Horizontal plane
AA expected for transmembrane NR insertion [a]	0.63	-0.5
AA expected for NR oriented parallel to membrane surface	-0.5	0.63
Average observed AA ±SD	0.12±0.30	-0.10±0.31
Number of pcNRs with transmembrane orientation [b]	5	1
Number of analyzed pcNRs	17	9

[a] Calculated based on the highest and lowest AA observed for all imaged pcNRs. The difference from 1 is because NR can be excited with light that is not in the plane of the main axis. The difference of the modules of values for vertical and horizontal plane are due to different intensity of the parallel and perpendicular light excitation.

[b] including those with tilt less than 30° (the difference of AA from expected values was less than (1-cos30°)×100%)

f. Cell culture and staining

HEK293 cells (AATC, VA) were maintained in 1:1 Dulbecco's Modified Eagle Medium and Nutrient Mixture F-12 (Invitrogen, NY) supplemented with 10% fetal bovine serum (FBS; Sigma-Aldrich, MO), 0.6 mg/ml of Geneticin (G418) (Life technologies), and 5μg/ml of puromycin (Life technologies). Cells were grown on 35mm glass bottom dishes until they reached 90 % confluency. The same protocol was applied to self-spiking HEK293 cells. For ANEPPS staining, di-8-ANEPPS solution in DMSO was added directly to the cells in a 35 mm glass bottom dish to a final concentration of 0.1 μM. Cells were then incubated at 4 °C for 5 mins before imaging.

After incubating for 10 minutes, a series of confocal cross-sections was taken by Leica SP-2 microscopy. Fig. 8 shows that the cell membranes are stained with pcNRs and pcQDs, respectively.

g. CryoEM control: Ligand-coated NRs do not insert into vesicles' membranes

As synthesized NRs were dissolved in toluene or hexane and precipitated by adding methanol multiple times to remove excess ligands. The NRs were then dissolved in DMSO and sonicated for 10 mins to minimize aggregation before adding to the vesicle solution (see Methods). 250 μl of the vesicle solution was extruded through a membrane with 100 nm pore size to facilitate formation of 100 nm SUVs, and 2 μl of the NR solution in DMSO was mixed with the extruded vesicle solution. The mix solution was then deposited on TEM grids and frozen according to the methods described in Methods. As shown in Fig. 9, the vesicles were not loaded with any NRs, indicating these NRs did not insert into the membrane of the vesicles.

h. Optical imaging and data acquisition of pcNRs' fluorescence signal in self-spiking HEK293 cells

The microscope set-up is based on an Olympus IX71 inverted microscope equipped with a Xenon lamp (Olympus, ULH75XEAPO, 75W) and excitation filter (BP 470/40, Chroma Technology Corp, Bellows Falls, VT). The excitation power is 2 mW at the image plane. The emission of the NPs was collected by a 60× objective lens (Olympus, PlanApo 60×, n=1.45, oil immersion) and passed through a dichroic mirror (DM, 505DCXRU, Chroma Technology Corp, Bellows Falls, VT). Imaging was done with an Andor iXon electron multiplying (EM) charge coupled device (CCD) camera (EMCCD, Andor iXon, South Windsor, CT). 2μl pcNRs in DMSO solution (~300 nM) were loaded to the glass-bottom dish (Fisher Scientific) where the self-spiking HEK293 cells were cultured. The pcNRs spontaneously inserted into cell membranes within 1-2 mins. The pcNR loading density estimated from the image is ~105 pcNRs per cell. After rapid shaking, the cell medium was changed with Dulbecco's Phosphate-Buffer Saline (DPBS, Life technologies). The dish was then placed on the microscope. Fluorescence was recorded in a movie format for 9 seconds with a 30 ms integration per frame.

i. Simultaneous patch-clamp recording and fluorescence imaging

2 μl of pcNRs were added directly to the cell culture (in a 35 mm glass bottom dish with 2 ml of cell culture medium). Cells were then incubated at 37 °C for 5 mins before patch-clamp and imaging. As estimated from images, about ~ 10 particles were inserted into each cell on average. The loading density is approximated to be ~ 10^{-7} pcNRs/nm^2. All imaging and electrophysiology were performed in Tyrode's buffer (containing 125 mM NaCl, 2.5 mM KCl, 3 mM $CaCl_2$, 1 mM $MgCl_2$, 10 mM HEPES, 30 mM glucose, at pH 7.3, and adjusted to 305-310 mOsm with sucrose). For patch clamp, filamented glass micropipettes (WPI) were pulled to a tip resistance of 5–10 MΩ, and filled with internal solution containing 125 mM potassium gluconate, 8 mM NaCl, 0.6 mM $MgCl_2$, 0.1 mM $CaCl_2$, 1 mM EGTA, 10 mM HEPES, 4 mM Mg-ATP, 0.4 mM Na-GTP (pH 7.3); adjusted to 295 mOsm with sucrose.

Pipettes were positioned with a Sutter MP285 manipulator. Whole-cell, voltage and current clamp recordings were acquired using a patch clamp amplifier (A-M Systems, Model 2400), filtered at 5 kHz with the internal filter and digitized with a National Instruments PCIE-6323 acquisition board at 10 kHz. Simultaneous whole-cell patch clamp recordings and fluorescence recordings were acquired on a home-built, inverted epifluorescence microscope equipped with a 60× water immersion objective, numerical aperture 1.20 (Olympus UIS2 UPlanSApo 60x/1.20 W), a long-pass dichroic filter (Chroma zt505-515+650NIR Tpc) and a scientific CMOS camera (Hamamatsu ORCA-Flash 4.0). 488 nm laser (Coherent Obis 488-50) intensity was modulated with an acousto-optic tunable filter (AOTF; Gooch and Housego 48058-2.5-.55-5W). Imaging of pcNRs was performed at illumination intensities of ~ 1 W cm^{-2}. For fast data acquisition, a small field-of-view around the cell of interest was chosen at the center of the camera to achieve a frame rate of 1,000 frames per second.

The data files used in the voltage sensing patch clamp experiment are freely available on figshare [61]. The dataset from the patch-clamp experiment consists of a video (272x192 pixels, 2000 frames at 400Hz or 2.5 ms per frame) and a synchronous set of electrical measurements (voltage, current) acquired by a DAQ interface at 10kHz. pcNRs positions with sub-pixel accuracy were manually identified in the above dataset by analyzing average frames on the raw video and on a temporal high-pass version of the video.

Data analysis was performed in python using the Jupyter/IPython Notebook (*56*) and a few common scientific libraries (numpy, scipy, matplotlib, pandas). The Jupyter notebooks are "live" (i.e. re-executable) documents that contain both a narrative description of the analysis, the code commands and the output (figures, text, links, etc ...). All the software used for data analysis of the patch-clamp experiment are open source and readily available on the internet.

The custom software used for patch-clamp data analysis is published in a public github repository: https://github.com/tritemio/voltagesensing where interested readers can find instructions on how to setup and reproduce the entire data analysis workflow. The repository contains a few .py files (python modules) containing low-level functions (data load, timetrace processing, burst search) and a set of Jupyter/IPython Notebooks that perform the full analysis. The notebook used in this paper can be also visualized online (read-only) at the following address: Patch Clamp Analysis - Phase offset-take1. Upon execution, the notebook generates an extensive set of plots of each analysis step and saves, in the *paper figures* folder, all the figures used in this publication (for the patch-clamp experiment). Finally, the raw unprocessed time-traces for each nanoparticle are saved in plain text format in the *results* folder in order to facilitate re-analysis with other tools.

From the datatset linked above, we manually identified pcNRs positions with sub-pixel accuracy, by analyzing average frames on the raw video and on a temporal high-pass version of the video. The notebook in section 3 of the link [61] contains figures of the center position of each identified pcNR for particles on the patched cell membrane (in the center of the field of view) and on unpatched cells' membranes. For brevity we will call these groups patched and unpatched pcNR.

A round ROI, centered on the pcNR position, is defined using a pixel radius of 1.8 pixels, resulting in a selection of roughly 20 pixels. Due to the pixel discretization and sub-pixel positioning of the pcNR the exact number of pixels selected for each particle can be slightly different. The notebook shows the exact ROI employed for each patched or unpatched pcNR (cells In [38] and In [39]).

(i) Optical recording of ANEPPS-labeled and pcNR-labeled spiking HEK cells

ANEPPS stained membrane regions of HEK cells were thresholded (= mean + standard deviation). White pixels in Fig. 10B are the area with intensity values that are larger than the threshold. Fig. 10C shows a temporal time trajectory for the spatial average of all white pixels in Fig. 10B, clearly exhibiting photo-bleaching. To remove this slowly varying contribution to the signal, we apply a 5th ($M=5$) order Butterworth-type high pass filter (HPF) with a cut-off frequency of $fc = 2.5$ Hz

$$HPF_{time}(f) = \sqrt{1 - \left(\frac{1}{\sqrt{(1 + f / f_c)^{2M}}} \right)^2}$$

The blue curve in Fig. 11D is the fast Fourier transform (FFT) of the signal shown in Fig. 11C and the green curve represents the above mentioned Butterworth HPF. The red curve in Fig. 11D represents the filtered signal (in the frequency domain). The black curve in Fig. 4D in time domain represents the filtered signal in the time domain.

In contrast to the ANEPPS staining, staining with pcNRs is non-uniform, leading to local bright areas with gradients of brightness (The left side of Fig. 4B is brighter than the right side). We applied a 10th order high pass Butterworth filter with 0.244 (pixel-1) as a spatial frequency (ω_c) cut-off. This filter removes the gradient and the cloudy background, increasing the visibility of single (or small aggregates) of pcNRs in Fig. 4C. Next, a simple threshold (= mean + 2 × standard deviation) is applied to obtain a binary image (Fig. 11C). Using this binary image as a mask, we calculate the intensity time trance averaged over these white pixels (Fig. 11D). Unlike the ANEPPS' result, the staining with pcNRs suffers from photo-brightening. To remove this slowly varying contribution to the signal, and the high-frequency shot-noise, we apply a 5th (M=5) order of Butterworth band pass filter (BPF) with flow = 2.5 Hz and fhigh = 7 Hz as cut-off frequencies

$$BPF_{time}(f) = \frac{1}{\sqrt{(1+f/f_{high})^{2M}}}\sqrt{1-\left(\frac{1}{\sqrt{(1+f/f_{low})^{2M}}}\right)^2}$$

The blue curve in Fig. 11E is the fast Fourier transform (FFT) of the temporal signal in fig. S8D and the green curve is the BPF function. The red curve in Fig. 11E represents the filtered signal (frequency domain). The filtered signal in the time domain is shown in Fig. 4F, black curve. The spiking cell analysis's data are freely available on figshare [62].

j. Data analysis of pcNRs' fluorescence during patch-clamp recording

From the video, the pcNRs' positions on both the patched cell membrane and on non-patched cells were manually identified. For each identified pcNRs, the time trace of emission intensity $\{t_k\}$ is obtained by averaging for each frame *k* a circular region of approximately 20 pixels around the pcNR. The time trace intensity is binned each 2 frames in order to obtain an intensity $\{\bar{t}_j\}$ for each voltage alternation semi-period, then the difference $\{\Delta F_i\}$ are computed as

$$\{(\bar{t}_1-\bar{t}_0),-(\bar{t}_2-\bar{t}_1),(\bar{t}_3-\bar{t}_2),-(\bar{t}_4-\bar{t}_3),\quad\}$$

(the signal alternates and is "+" for ON-OFF and "-" for OFF-ON transitions). Finally, these differences are divided by the average time trace intensity to obtain the signal $\{\Delta F_i/F\}$.

The signal $\{\Delta F_i/F\}$, the normalized version (where F is the average time-trace value) and several derived statistics are computed both for particles in the patched cell membrane (patched set) and for particle in other position of the field of view (unpatched set).

A burst search analysis is performed to complement the modulated signal analysis by focusing on the brief periods of high signal in a time-trace, instead of performing averages on the full time-trace. The motivation behind this type of analysis is to better discriminate the small, transient signal from the background under the assumption that pcNRs experience brief periods of transient insertion into/out of the membrane. The goal of burst search is detecting the time periods during which the fluorescent signal alternates in phase with the modulating voltage.

The burst search is performed as follows. The square of the running average of the modulation response $\{\Delta F_i/F\}$ is computed and the time periods where this squared average is higher than a threshold (set to 60% of the maximum) are identified as bursts. Next, for each burst i, we extracted the total signal (burst score)

$$S_i=\frac{1}{F}\sum_i \Delta F_i$$

The quantity represents the total amount of modulated signal present in each burst. In principle, the burst score can be either positive or negative, depending on whether the fluorescence intensity increases or decreases when the voltage is applied. For the pcNRs employed here, the fluorescence is decreased. This is consistent with the observed excess of bursts with negative score for the selected particles on the patched cell membrane.

As a control, an out-of-phase version of $\{\Delta F_i\}$ is computed by simply removing the first frame from the raw time-trace prior to the other processing steps. In this case, when computing the 2- element block average to obtain the reduced time-traces, the frame removal results in averaging one ON and one OFF semi-period frame. As a consequence, intensity variations due to the voltage modulations are suppressed. The distribution of out-of-phase $\{\Delta F_i\}$ values has a theoretical mean of zero and a standard deviation that is a characteristic of the background.

More specifically, the out-of-phase response is obtained by removing the first video frame and applying the same analysis on the time traces. In this case, the binning step averages frames between ON and OFF semi-periods, suppressing any signal in-phase with the voltage alternation.

Histograms of the in-phase and out-of-phase signal distributions are reported in notebook section 8 (link) (61,62). Several statistics for the alternated differences $\{\Delta F_i\}$ are reported in the notebook (i.e. mean, standard deviation, mean/standard deviation, mean/(mean intensity)). Here, in Fig. 12, we show the mean signal for different pcNRs. We note that among the patched pcNRs in positions #0, #1, #3, #4 and #8 exhibit significantly higher signal than the out-of-phase signal and the signals for unpatched particles. However, the pair of positions #0 - #1 (and #3 - #4), have pixels in common (i.e. the ROIs overlap) and show highly correlated time-traces, indicating that the signals are originated from the same particles (or small cluster of particles). In order to avoid treating those pairs as separate particles (and over-representing those positions which exhibit high signal), we discard positions #0 and #3 in the following analysis steps.

Fig. 13A and 13B show aggregated results for patched and unpatched NPs, both for in-phase and out-of-phase signal. In Fig. 13A we show the full distribution for the 4 cases, whereas Fig. 13B shows the distribution mean and the $\pm 1\sigma$ error range (computed under assumption of Gaussian distribution). We note that only the in-phase signal for the "patched" set exhibits a statistically significant deviation from 0. The full distribution shows also a larger negative tail for the patched in-phase signal suggesting that there may be a few temporally interspersed "bursts" of negative signal.

k. Time-trace extraction, filtering and blinking removal

For each identified pcNR, we compute the time-trace by averaging the signal in each ROI for each frame. Each of these raw time-traces is a 2000-element array, each element corresponding to a single video frame (the first 4 frames are discarded on loading since they systematically contain corrupted data due to specificities of the acquisition system). The voltage modulation has a period of 4 frames, of which the first 2 correspond to voltage-on and the last 2 to voltage-off semi-periods. Raw and processed timetraces are shown in the notebook section 4 (link) [61].

In order to remove the time intervals where the pcNR is not fluorescent (due to blinking), a threshold is usually applied. In the present case, a slow-varying drift in the raw time-traces (1 s time scale) makes it difficult to identify a meaningful threshold. Therefore, we first apply a filter that removes the slow (low frequency) variations in the time-trace. This filter is a high-pass Gaussian filter with sigma of 300 frames (750 ms, see notebook figure In[42]). Next, we smooth the time-trace by applying a low-pass filter (Gaussian filter with sigma=10 frames, 25ms) in order to better identify the switch-points related to the particle fluorescence intermittency (blinking). Due to noise, without this smoothing step, we could erroneously detect multiple spurious ON/OFF transitions in correspondence with a single switch-point. Figures of the filtered time- traces overlaid with the smoothed version used to identify the blinking periods are shown in the notebook section 4 (figures In[44] and In[45]) in the data file link [61].

Finally, the dark-state periods are removed from each time-trace, making sure that a 4 frames alignment is preserved so that the reduced time-traces are still in phase with the alternation signal. This operation is performed by two python function: the function `get_on_periods_slices()` (link) performs the quantization to multiple of 4 frames for the start-stop index of each ON blinking period; `get_on_periods_timetrace()` (link) performs the stitching of the ON blinking periods in the time-traces.

I. Simulation of the energetics of the NR in the membrane

Since the energy of any nanorod configuration in the membrane is determined by the areas of hydrophobic and hydrophilic surfaces in contact with the interior of the membrane and (aqueous) solvent, the energy calculation can be performed using a geometrical analysis. In this section we outline calculation f the various areas involved in determining the nanorod insertion energy. We use these calculations to address two points. First, we examine the orientational stability of rods in the membrane by computing their mean tilt (or canting) angle with respect to the membrane local normal. We also consider the thermal fluctuations of that tilting angle. Secondly, we consider the equilibrium partitioning of the nanorods between the solvent and the membranes, and find that for almost all hydrophobic (hydrophilic) energy scales and nanorod dimensions, the rods will strongly partition to the membrane.

(1) Geometry of the nanorod in the membrane

In the frame of the rod or radius a and length L, the points on the surface of the rod are given by

$$\hat{r} = a\cos\phi\hat{x}' + a\sin\phi\hat{y}' + \rho\hat{z}' \qquad 7.1$$

where r < L / 2 and the azimuthal angle f covers the unit circle, $-\pi \leq \Phi < \pi$. In the reference frame where the membrane (of thickness t) has unit normal n = z and occupies the space |z| < t / 2, the nanorod is oriented so that its symmetry axis lies along p, p x n = cosθ and has its center at height h above the midplane of the membrane – see Fig. 14A for a schematic representation of the configuration in terms of these degrees of freedom. Putting the nanorod in the xz-plane (without loss of generality) the surface of the cylinder lies on

$$\mathbf{r} = \hat{x}\left[\rho\sin\theta - a\cos\theta\cos\phi\right] + \hat{y}a\sin\phi + \hat{z}\left[h + \rho\cos\theta + a\sin\theta\cos\phi\right] \qquad 7.2$$

where ρ and <u>Φ</u> range over the same intervals as above. We neglect the endcaps of the cylinder for now.

The curve defining the intersection of the cylinder with the upper boundary of the membrane z = t/2 is given by

$$\rho_{up}^{(0)}(\phi) = \frac{t}{2\cos\theta} - \frac{h}{\cos\theta} - a\tan\theta\cos\phi \qquad 7.3$$

Since the ends of the cylinder may be in the interior of membrane, the upper limit of ρ is actually

$$\rho_{top}(\phi) = \min\left[\frac{L}{2}, \rho_{top}^{(0)}(\phi)\right] \qquad 7.4$$

For certain values of the vertical displacement h and tilt angle θ, the top of the cylinder is buried in the membrane, at least for some azimuthal angles Φ.

Similar considerations apply to the set of points on the cylinder where it intersects the lower edge of the membrane. These points are defined by

$$\rho_{bottom}^{(0)}(\phi) = -\frac{t}{2\cos\theta} - \frac{h}{\cos\theta} - a\tan\theta\cos\phi \qquad 7.5$$

As discussed with regard to Eq. 7.4, some of these points may be off the lower end of the cylinder when all or part of the bottom of the cylinder is buried in the membrane. To account for this case, we must use a lower limit given by

$$\rho_{bottom}(\phi) = \max\left[-\frac{L}{2}, \rho_{top}^{(0)}(\phi)\right] \qquad 7.6$$

To compute the surface area of the rod enclosed in the membrane, we integrate over the surface using the limits of integration obtained above in Eq. 7.4 and 7.6

$$A = \int_{-\pi}^{\pi} a\,d\phi \int_{\rho_{bottom}(\phi)}^{\rho_{top}(\phi)} d\rho\,\Theta(\rho,\theta,h,\phi) \qquad 7.7$$

where we include in the integrand Θ, which vanishes if the bottom of the cylinder is above the upper edge of the membrane or if the top of the cylinder is below its lower edge.

The above analysis is designed to account for the central hydrophobic part of the cylinder, which is of length L. It is, however, the amount of hydrophilic surface area inside and outside the membrane can be accounted for by redoing the above analysis with different ranges of ρ. Specifically, to account for the upper hydrophilic part of the cylinder of length b, we shift the range of ρ to $(L / 2 , \ L / 2 + b)$. The lower hydrophilic cylinder is corresponds to a range of ρ given by $(- b - L / 2 , \ - L / 2)$.

(2) Energetics of the nanorod in the membrane

The energy of the nanorod is directly determined by four surface energies. We define $\gamma_c^{\omega,o}$ to be the surface energies, measured in units of k_BT / nm^2 of central hydrophobic rod in water (w) or in the oily (o) interior of the membrane $\gamma_c^o < \gamma_c^{\omega}$

We define two analogous surface energies for the outer hydrophilic parts of the rod, $\gamma_o^{\omega,o}$ where now $\gamma_o^{\omega} < \gamma_0^{0}$.

(n) Height and orientational fluctuations of rods in the membrane

Because of the various geometrically required inequalities obeyed by the integration variables it is difficult to provide a generic, closed-form solution for the energy of the nanorod in the membrane $\varepsilon(\theta,h)$. Instead, we examine a specific case with L = 8 nm, a = 2 nm, b = 2 nm, and a membrane of thickness t = 4 nm. In units of k_BT/ nm^2, we take

$$\gamma_c^{\omega} = 2.0, \gamma_c^{o} = 0.1, \gamma_o^{\omega} = 0.1, \gamma_o^{o} = 1.0$$

The energy surface is shown in Fig. 14C.

There are two distinct features of this energy surface, both of which are attributable to the mismatch of the hydrophobic center to the membrane thickness. First, when we consider the potential along the h axis at a fixed canting angle θ, it is initially flat – small vertical displacements of nanorod do not change the energy as the hydrophobic section is longer than the width of the membrane. Once, the vertical displacement is sufficiently large so as to begin to bury the hydrophilic ends of the rod, the potential increases rapidly in a nearly linear fashion until the rod leaves the membrane entirely.

Second, when we consider the energy surface in the tilting (theta) direction near symmetric insertion ($h = 0$), we see that the hydrophobic mismatch between the central part of the rod and the membrane thickness leads to a decrease of energy with increasing angle. As the rod tilts, more hydrophobic surface is buried within the membrane lowering the total energy of the system. When the hydrophilic top or bottom of the rod touches the membrane, however, this energy reduction with increasing angle is arrested as it become energetically unfavorable to bury more and more of the hydrophilic ends inside the membrane. A local minimum in the energy appears at an angle which depends on the various surface energies of the two regions. We see then that the orientation of the rod along the local membrane normal is unstable to canting as a result of the hydrophobic mismatch. We will see below that, even in cases of zero hydrophobic mismatch, nonzero canting angles are still favored, now solely due to entropic considerations.

For the special case of zero hydrophobic mismatch, the rod is strongly pinned within the membrane, i.e., with h near zero. The effective potential for rod canting (i.e., angling with respect to the local membrane normal) is effectively linear in the angle ~ $a\theta$, with $a \sim O(10K_BT)$ for typical values for nm scale rod dimensions and surface energies of a few

$k_BT/\ nm^2$. Thus the mean canting angle of the rod is approximately given by

$$\langle\theta\rangle \approx -\partial_a \log\left[\int_0^\infty e^{-a\theta} \sin\theta\right] = \frac{2a}{1+a^2} \qquad 7.8$$

where, noting the rapid decay of the Boltzmann factor for larger angles, we have extended the upper limit of the integrand to infinity. As the potential is made steeper by, e.g., increasing the hydrophobic energy of the interior segment of the rod, the mean angle goes to zero as 2/a. This angle represents the competition between the energy cost for canting due to the burial in the membrane of the rod's hydrophilic ends and exposure of its hydrophobic interior to the surrounding solvent with the increased orientational phase space associated with larger canting angles.

The fluctuations about this mean value are given by

$$\left\langle \theta^2 \right\rangle - \left\langle \theta \right\rangle^2 \approx -\partial_a^2 \log\left[\int_0^\infty e^{-a\theta} \sin\theta\right] \approx \frac{2}{a^2} \tag{7.9}$$

in the region of interest. Thus, nanorods with no hydrophobic mismatch typically lie at small angles with respect to the membrane normal, <θ> ~0.2~10 and exhibit small fluctuations about this angle that are comparable to this angle:

$$\sqrt{\left\langle \theta^2 \right\rangle - \left\langle \theta \right\rangle^2} \sim \left\langle \theta \right\rangle$$

Given the similarity of the geometry of these nanorods to transmembrane proteins and their aggregates, we expect similar equilibrium orientations and fluctuations for them as well.

The key determinant of the canting angle distribution and the propensity for the nanorods to lie in the plane of the membrane θ ≈ π/2 appears to be the amount of hydrophobic mismatch-- the difference in the thickness of the hydrophobic layer on the rod and the thickness of the membrane. In Fig. 2G we show the probability distribution for rod canting angles in the membrane for two rod geometries. In the first case (blue) the hydrophobic mismatch is zero; the length of hydrophobic section of the rod is equal to the membrane thickness L = t = 4 nm. Here we see a maximum in the angle probability distribution at angles comparable to the (small) mean canting angle <θ> as computed from Eq. 7.8. In the second case (red), the hydrophobic section of the rod extends significantly beyond the boundaries of the membrane: L = 6 nm, while t = 4 nm. One observes that the local maximum in the probability distribution has moved to larger angles, with a maximum at a canting angle of θ ≈ 0.6, but there a new local maximum has developed for the case of the rod lying in the plane of the membrane, θ ≈ π/2. Sufficient hydrophobic mismatch will destabilize the (nearly) normal insertion orientation of the rods making them transmembrane poor voltage sensors. In both cases shown here (red and blue) the hydrophilic ends of the cylinder are 2nm long and all hydrophobic and hydrophilic surface energies are identical.

(3) Partitioning of nanorod between solvent and membrane

To determine the equilibrium partitioning of nanorods between the membrane and surrounding fluid, we compare the partition function associated with a nanorod in aqueous solution of volume V

$$Z_{water} = 4\pi V \exp\left[-\left(4\pi ab\gamma_o^{w} + 2\pi aL\gamma_c^{w}\right)/k_BT\right]$$

7.10

with the partition function associated with the rod being in membrane of surface area A

$$Z_{membrane} = 4\pi A\int_0^{+1} d\cos(\theta)\int_{h_{min}}^{h_{max}} dh e^{-E(\theta,h)/k_BT}$$

7.11

In Eq. 7.10 the prefactor of 4πV accounts for the orientational and translational degrees of freedom of the rod. These factors of are similarly accounted for in Eq. 7.11 by the prefactor of 2 x 2πA . The first factor or two allows for the insertion of the rod in either of its two (identical) orientations. The remaining integrations in that equation are over the degrees of freedom determining the orientation of the rod in the membrane. The height integral is limited to hmin(θ) and hmax(θ) determined so that at least some part of the rod is in contact with the membrane.

We define the partitioning fraction of the nanorods R as the fraction of nanorods in the membrane of spherical vesicles of radius R at number density n. From Eqs. 7.10, 7.11, this fraction is given by

$$\mathcal{R} = \frac{r}{1+r} \qquad 7.12$$

where r is the ratio of the two partition sums given above: r = Zmembrane/Zwater. Taking these partition sums from Eqs. 7.10, 7.11, we find

$$r = 4\pi\mathfrak{R}^2 n \exp\left[\left(4\pi ab\gamma_s^w + 2paL\gamma_s^e\right)/k_BT\right]\int_0^{+1} d\cos(\theta)\int_{h_{min}}^{h_{max}} dh \exp\left[-\varepsilon(\theta,h)/k_BT\right] \qquad 7.13$$

The partitioning of the nanorods between the membrane and the solvent is controlled mainly by the hydrophobicity of the central part of the nanorod and the concentration of vesicles in solution. As long as these hydrophobic energies are significant, i.e., on the order of k B T / nm 2 and the concentration of vesicles is at least in the nM (nanoMolar) regime, essentially all of the nanorods will be inserted into membranes in thermal equilibrium.

One may see this result from a simple estimate of the r factor defined in Eq. 7.13. To simplify the calculation, we assume that the energy difference between the rod in the membrane and in the (aqueous) solvent is due solely to the exposure of the hydrophobic surface of the nanorod to water when in solution. Taking the length of the rod to be equal to the membrane thickness t, this Boltzmann weight associated with this energy difference is

$$\exp\left[2\pi a t \gamma_c^{\infty}\right] \sim 10^{28}$$

Taking there to be only N ~ 10^9 vesicles (of micron radius: R = 1 μm) per liter, we find the estimate for r to be

$$r \sim \frac{\Re^2 t N e^{2\pi a t \gamma_c^{\infty}/k_B T}}{v} = 10^{14} \qquad 7.14$$

This estimate assumes that the excess energy cost of putting 1 nm^2 of hydrophobic surface in contact with water instead of the lipid membrane interior is 1 k_BT. Because of the exponential dependence of the result on this hydrophobic energy cost, reducing that energy difference to ~ 0.3 k_BT per nm^2, results in r ~ O (1) , implying a roughly equal partitioning of the nanorods between membrane and solvent, at least at this low membrane concentration.

7. Advantages and Improvements

NRs possess many advantages over organic fluorophores, having inherently large voltage sensitivity, large absorption cross-section, and reduced photobleaching. However, they are difficult to integrate into biological and neuroscience applications due to their large size and unknown surface properties that leads to non-specific binding. Furthermore, inserting NRs into membrane bilayers presents additional challenges due to the need for sophisticated facet-selective surface functionalization for control of insertion orientation.

In this study, the inventors showed membrane insertion of pcNRs, utilizing alpha-helical peptides as the NRs' surface ligand, as clearly demonstrated by TEM micrograph (Fig. 2A). Based on these observations and on a statistical mechanics-based theoretical investigation (Fig. 2E and section 6I.), the inventors conclude that > 60% of all membrane associated pcNRs are favorably oriented (long axis parallel to the membrane's normal), but not necessarily fully inserted into the membrane. The polarization microscopy experiment also reveals that the subpopulation of NRs in GUVs are oriented in a favorable orientation (Fig. 6). For highest voltage sensitivity, however, pcNRs need to be aligned as parallel to the membrane normal as possible (to guarantee maximal QCSE charge separation) with both tips exposed to the cytoplasm and to the extracellular matrix respectively. The small fraction (~16 % of all geometry) of NRs, indeed, prove the proper insertion in the membrane, showing the feasibility of membrane potential sensing. Importantly, fluorescence signals could be recorded from individual membrane-inserted or associated pcNRs, as is evident from the typical temporal blinking (intermittency) pattern (*49*) in their emission (Movie S1). The high brightness of pcNRs stems from their large absorption cross-section and high emission quantum yield (*50*). A scientific complementary metal-oxide semiconductor (sCMOS) camera and a 488 nm laser (see Material and Methods) were used in the patch-clamp experiment. With this optical system, the camera can be operated at a 400 Hz frame rate (2.5 ms integration time per frame) while capturing the modulated signal. The present disclosure estimates that, if an electron multiplying charge coupled device (EMCCD) camera is used instead together with shorter wavelength laser excitation (< 450nm), the higher NR's emission rate and the higher camera gain will result in a higher S/N. Together, shorter wavelength laser excitation and EM gain will yield higher S/N, allowing for an acquisition rate of ~1 kHz, but at the expense of working with a smaller region of interest through binning (since EMCCD camera acquisition rates are usually slower than those of sCMOS cameras). The NR's absorption cross-section could be further increased by adopting a lower bandgap material (illustrative embodiments disclosed herein used NRs consisting of a CdSe seed and a CdS shell with an optical bandgap of 600 nm). Using bandgap engineering and a different choice of materials' composition, the bandgap could be lowered towards the near IR, while excitation could be tuned to the blue/near UV region of the spectrum. This will lead, in return, to an even higher single NR brightness. The inventors believe that by further improving the optical set up and the NR's photon emission rate, it should be possible to record signals from individual NRs at > 1 kHz rate, and hence capture individual action potential spikes. Moreover, an increased photon emission rate allows implementation of advanced noise-immune voltage sensing techniques such as lifetime imaging, spectrally separated ratiometric measurement, or a spectral shift measurement. These approaches are to a large extent immune to fluorescence intermittency. The simple intensity-based measurement reported here, on the other hand, is highly sensitive to intermittency and therefore required filtering of the raw signals.

Overall, the illustrative results presented herein demonstrate that an individual pcNR, or a small aggregate of pcNRs, is capable of recording the membrane potential. The reduced voltage sensitivity of an ensemble of membrane inserted pcNRs in self-spiking HEK293 cells (Fig. 4F, $\Delta F/F$ ~0.6 %) as compared to the sensitivity of ANEPPS (a typical VSD exhibiting $\Delta F/F$~10% in Fig. 4D) is attributed to imperfect membrane insertion for a large fraction of the pcNRs. However, as the study of the interaction energy between a NR and its environment (solvent and a membrane) estimates the NR's orientation quite accurately (Fig. 2C~E), the optimized geometry for membrane insertion can be drawn with further theoretical investigation. To achieve stable and robust PL signal, more advanced surface functionalization can be implemented, e.g., exploiting the different surface energy between a NR's cylinder wall and its tips and employing face-selective surfactants (hydrophilic surfactants at the NR's tips). Nonetheless, even with the current generation of NRs and coating, a small fraction (~16%) of individual or small aggregates NRs exhibiting a sizeable $\Delta F/F$ ~5.0 % can be found.

Fig. 4F and G show larger than 5 % signal is intermittently captured and that the individual NR's typically averaged $\Delta F/F$ ~1 %. This is likely due to the blinking feature of the NR and its dynamic movement/ orientation fluctuation in the membrane. However, as non-blinking nanocrystals are currently introduced, the PL fluctuation due to blinking will be improved (*52*).

In a second experiment, a voltage modulation of -150 mV to 0 mV (somewhat larger than a typical action potential, -70 mV to 40 mV) was applied to a patched (wild-type) HEK cell. Under this modulation, the inventors were able to observe a higher in-phase pcNRs' modulation response that is statistically significant as compared to unpatched cells, whereas the control experiment (out-of-phase analysis) showed no modulation response as expected (Fig. 5C). The sensitivity, the noise level, and the temporal resolution of these measurements may be optimized for electrophysiological recording.

The data presented in Figs. 4 and 5 suggest that pcNRs could be suitable for membrane potential recording. Marshall et al., estimated 5% and 30% of $\Delta F/F$ during neuronal spiking with type-I and type-II QDs, respectively (*34*). The signal quality could be greatly increased by a series of enhancements. For example, preliminary experiments and calculations suggest that seeded nanorods heterostructures with type-II band offset and large seed position asymmetry could exhibit very high voltage sensitivity (*33*). Moreover, improved membrane insertion stability will reduce measurement noise and enhance the signal. Lastly, as previously shown (*33*), shifts in spectral peak position are considerably more sensitive than $\Delta F/F$ changes. Simple modification to the optical set-up (based on "dual-view" microscopy (*53*)) could enhance voltage sensitivity even further.

Further information on design rules for membrane-embedded voltage-sensing nanoparticles used in one or more embodiments of the invention can be found in [53].

8. Example Applications

Development of high sensitivity pcNRs could afford unprecedented ways for studying

electrical activities in neuronal, neuromuscular, cardio, and visual systems on the nanoscale (such as across a single synapse) or the ability to record a large number of signals from a large-field of view (high throughput recording). pcNRs could also find applications in other areas of science and engineering, as for example, in inducing action potential (*54, 55*), characterization of highdensity fast integrated circuits, and energy harvesting by membrane-inserted artificial light harvesting complexes. Lastly, the ability to impart membrane protein-like properties to inorganic and organic nanoparticles could allow the construction of novel membrane-based hybrid (organic-inorganic) materials with unique exploitable properties.

9. Process Steps

a. Composition of matter

Fig. 15 is a flowchart illustrating a method of making a composition of matter.

Block 1500 represents forming or obtaining peptides 102. The peptides each comprise a hydrophilic segment 106 connected to a lipophilic segment 108. The segments comprise cysteine residues. In one or more examples, the peptides or molecules are considered large enough to be considered proteins.

Block 1502 represents attaching the peptides to a semiconductor nanorod 104 or nanoparticle, wherein the hydrophilic segment attaches to an end of the semiconductor nanorod, the lipophilic segment attaches to a side of the semiconductor nanorod, and the cysteine residues mediate attachment of the peptides to the semiconductor nanorod. One of ordinary skill in the art understands that a variety of peptides or proteins can be used and adapted for the purposes described herein, e.g., for rendering the nanorod(s) protein-like and/or for functionalizing the nanrods to favor stable, spontaneous, insertion of the nanorod(s) into a cell membrane with the correct vertical orientation for the sensing applications described herein.

Block 1504 represents the end result, the composition of matter. The composition of matter can be embodied in many ways including, but not limited to, the following embodiments.

2. A composition of matter 100 comprising peptides 102 attached to a semiconductor nanorod 104 or nanoparticle, wherein the peptides 102 each comprise a hydrophilic segment 106 connected to a lipophilic segment 108, the lipophilic and hydrophilic segments 106, 108 comprise cysteine residues 110, the hydrophilic segment 106 attaches to an end 112 of the semiconductor nanorod 104, the lipophilic segment 108 attaches to a side 114 of the semiconductor nanorod 104, and the cysteine residues 110 mediate attachment of the peptides 102 to the semiconductor nanorod 104.

2. The composition of matter of embodiment 1, wherein the peptides 102 each comprise the lipophilic segment 108 terminated by a fatty acid 116.

3. The composition of matter of one or any combination of the preceding embodiments, wherein the liphophilic segment 108 comprises an alpha-helix structure 118.

4. The composition of matter of one or any combination of embodiments 1-2 wherein the cysteine residues 110 are disposed in an alpha-helix structure 118 so that a

side 120 of the alpha-helix structure facing the semiconductor nanorod 104 is cysteine rich and a side 122 of the alpha-helix structure 118 facing an exterior is lipophilic.

5. The composition of matter of one or any combination of embodiments 1-3, wherein the hydrophilic segment 106 comprises a flexible unstructured domain 124 (non-helical structure) that bends around the end 112 of the nanorod 104.

6. The composition of matter of one or any combination of embodiments 1-4, wherein the peptides each comprise residues 126 that preferentially localize at a membrane-water interface.

7. The composition of matter of any combination of embodiments 1-5, wherein each of the peptides further comprise a segment of aliphatic amino acids that prevent aggregation of the peptides in solution.

8. The composition of matter of embodiment 6, wherein the aliphatic amino acids comprise a hydroxyl-containing Thr residue and an acidic residue.

9. The composition of matter of one or any combination of embodiments 1-7, wherein a sequence of each of the peptides is Myristoyl-CLTCALTCMECTLKCWYKRGCRGCG-COOH (SEQ ID NO:1) wherein the hydrophilic segment comprises KRGCRGCG (SEQ ID NO:2). However, other sequences are possible. One of ordinary skill in the art understands that protein compositions or sequences that achieve the one or more functionalities describes herein for proper membrane insertion may be used.

10. The composition of matter of one or any of combination of embodiments 1-8, wherein the peptides comprise between 2 and 20 peptide chains disposed around the nanorod,

the hydrophilic segment comprises less cysteine residues (e.g., less than 5) as compared to the lipophilic segment (e.g., more than 5), and each peptide extends over at least half the length of the nanorod.

11. The composition of matter of one or any combination of embodiments 1-10, wherein the semiconductor nanorod has a length L in a range of 5 – 50 nm and a W width in a range of 1- 10 nm.

12. The composition of matter of one or any combination any of embodiments 1-11 inserted into a cell membrane 200, wherein the semiconductor nanorod 104 has a length L longer than a thickness T of the cell membrane.

13. The composition of matter of one or any combination of embodiments 1-12 inserted into a cell membrane 200, wherein the cell membrane is a lipid bilayer.

14. The composition of matter of one or any combination of embodiments 1-13, wherein the semiconductor nanorod 104 comprises at least one material selected from CdSe and ZnSe-CdS.

15. The composition of matter of one or any combination of embodiments 1-14, wherein the semiconductor nanoparticle or nanorod 104 comprises a semiconductor having a type II band offset.

16. The composition of matter of one or any of embodiments 1-15, wherein the semiconductor nanorod 104 has a bandgap in a range of 0.6 eV - 1.77 eV.

17. A composition of matter, comprising peptides 102 attached to a semiconductor nanorod 104, wherein the peptides each comprise a helical 118 and a flexible part 124 binding different faces F1, F2 of the nanorod 104. The helical part faces face F1 on a side 114 of the nanorod and the flexible part faces face F2 on a side 112 of the nanorod.

b. Apparatus

Fig. 16 illustrates a method of fabricating an apparatus 900 for measuring a membrane potential (also referring to Fig. 17).

Block 1600 represents positioning a camera 1714 or detector for measuring one or more changes in fluorescence 1716 emitted from one or more peptide coated nanorods 100 inserted in a cell membrane 200 when the nanorods are excited with electromagnetic radiation 1718.

Block 1602 represents providing a computer 1702 or coupling the computer to the camera 1714, wherein the computer filters the fluorescence 1716 so as to extract the response from noise, and determines one or more magnitudes and/or one or more waveforms of the membrane potentials from the response.

The computer 1702 comprises a processor 1704 (general purpose processor 1704A and special purpose processor 1704B) and a memory, such as random access memory (RAM) 1706. Generally, the computer 1702 operates under control of an operating system 1708 stored in the memory 1706, and interfaces with the user/other computers to accept inputs and commands (e.g., analog or digital signals) and to present results through an input/output (I/O) module 1710. The computer program application 1712 accesses and manipulates data stored in the memory 1706 of the computer 1702. The operating system 1708 and the computer program 1712 are comprised of instructions which, when read and executed by the computer 1702, cause the computer 1702 to perform the operations herein described. In one embodiment, instructions implementing the operating system 1708 and the computer program 1712 are tangibly embodied in the memory 1706, thereby making one or more computer program products or articles of manufacture capable of controlling the electromagnetic radiation and performing the data analysis methods described herein. As such, the terms "article of manufacture," "program storage device" and "computer program product" as used herein are intended to encompass a computer program accessible from any computer readable device or media. In one or more examples, the computer program is implemented in a numerical control programming language.

Block 1604 represents optionally positioning or providing a source of electromagnetic radiation 1710 so as to irradiate the nanorods.

Block 1606 represents the end result, the apparatus 1700. The apparatus can be embodied in many ways including, but not limited to, the following embodiments.

1. An apparatus 1700 for measuring a membrane potential, comprising a camera 1714 measuring one or more changes in fluorescence 1716 emitted from one or more peptide coated nanorods 104 inserted in a cell membrane 200 when the nanorods are excited with electromagnetic radiation 1718. Examples of changes in fluorescence include change in fluorescence intensity, change in fluorescence emission wavelength, and/or change in fluorescence lifetime. The one or more changes include a response to one or more membrane potentials applied to the one or more nanorods by the cell membrane, the one or more nanorods each have a long axis A substantially parallel to the cell membrane's normal, and the one or more nanorods each protrude from both sides of the cell membrane. The computer 1702 coupled to the camera filters the fluorescence so as to extract the response from noise, and determines one or more magnitudes and/or one or more waveforms of the membrane potentials from the response.

2. The apparatus for measuring the membrane potential of embodiment 1, wherein the camera 1714 measures the fluorescence comprising a wavelength shift in response to the membrane potentials, and the computer determines the one or more magnitudes and/or one or more waveforms by modeling the wavelength shift as a Quantum Confined Stark Effect.

3. The apparatus of one or any combination of embodiments 1-2, further comprising the source (e.g., laser 1716) of the electromagnetic radiation 1718 comprising blue and/or ultraviolet (UV) electromagnetic radiation (a

wavelength in a range of 350 nm – 1 micron). The nanorods 104 emit the fluorescence 1716 in response to being excited with the electromagnetic radiation when the membrane potentials are being applied to the nanorods.

4. The apparatus of one or any of combination of embodiments 1-3, wherein the camera measures the fluorescence with an acquisition rate of more than 1 Hz -5 kHz.

5. The apparatus of one or any combination of embodiments 1-4, wherein the camera comprises an electronic imaging sensor detecting the fluorescence.

6. The apparatus of one or any combination of embodiments 1-5, wherein the computer determines the one or more magnitudes and/or waveforms of the membrane potentials from the fluorescence emitted from a single nanorod.

7. The apparatus of one or any combination of embodiments 1-6, wherein the nanorods comprise the composition of matter 100 of one or any combination of embodiments 1-17 of the composition of matter described above.

Those skilled in the art will recognize many modifications may be made to this configuration without departing from the scope of the present disclosure. For example, those skilled in the art will recognize that any combination of the above components, or any number of different components, peripherals, and other devices, may be used.

c. Method of measuring

Fig. 18 is a flowchart illustrating a method of measuring a membrane potential.

Block 1800 represents obtaining or disposing/placing/depositing nanorods on or in a cell membrane so that the nanorods self assemble and insert into the cell membrane.

Block 1802 represents obtaining fluorescence (e.g., a fluorescence image) of the nanorods inserted in the cell membrane. The step may comprise obtaining the fluorescence in response to irradiating the nanorods in cell membrane with electromagnetic radiation.

Block 1804 represents processing the image or filtering the fluorescence. The filtering may comprise filtering so as to extract one or more signals from noise, wherein the one or more signals correspond to one or more changes in the fluorescence emitted from one or more peptide coated nanorods (e.g., composition of matter of one or any combination of the composition of matter embodiments 1-17 described above) inserted in a cell membrane (e.g., lipid bilayer), the one or more changes are in response to one or more membrane potentials applied to the one or more nanorods by the cell membrane, the one or more nanorods each have a long axis substantially parallel to the cell membrane's normal, and the one or more nanorods each protrude from both sides of the cell membrane.

In one or more examples, the processing may comprise processing the image so as to identify the signal comprising a single diffraction limited fluorescence spot. In one or more examples, the fluorescence spot corresponds to fluorescence from a single nanorod.

Block 1806 represents determining (e.g., in a computer or processor) one or more magnitudes and/or one or more waveforms of the membrane potentials (e.g., voltage potentials) from the one or more signals.

Block 1808 represents outputting the using the membrane potentials (e.g., voltage potentials) in an application, e.g., to measure or sense a cellular process or treat or diagnose a disease, for example, or fabricate a therapeutic device.

Examples of cellular processes that can be sensed include, but are not limited to, neuronal signals, action potentials, membrane potential sub-threshold events, membrane potentials of cardiomyocytes, opening and closing of ion channels, ionic currents in ion channels, and vesicle fusion and neurotransmitters release. Thus, the NPs according to embodiments of the present invention have wide ranging applicability, including as research tool for cellular voltage studies, as a diagnostic tool, or as a therapeutic device. In one bioelectronics implementation, the membrane potential data could be used to correct aberrant neuronal signals. In another example, the NPs could be used to stimulate the neurons (e.g., as a neuro-implant) by generating photo-voltaic charges. In yet another implementation, the NPs could be used to image arrhythmia and guide the ablation procedure. In yet a further implementation, the NPs could be injected into the eye and be inserted into retina cell membranes so that upon light absorption, the NPs actuate neuronal signals and thus restore vision.

In one or more examples, the method is implemented using the apparatus of one or any combination of embodiments 1-7 described above.

Further information on one or more embodiments of the present invention can be found in (63).

10. Sequence for peptide described herein.

a. Peptide (SEQ ID NO:1)
CLTCALTCMECTLKCWYKRGCRGCG

b. Peptide (SEQ ID NO:2)
KRGCRGCG

c. Peptide (SEQ ID NO:3)
KCWYK

References

The following references are incorporated by reference herein.

1. C. B. Murray, D. J. Norris, M. G. Bawendi, Synthesis and characterization of nearly monodisperse CdE (E = sulfur, selenium, tellurium) semiconductor nanocrystallites. *Journal of the American Chemical Society* **115**, 8706 (1993/09/01, 1993).

2. X. Peng, L. Manna, W. Yang, J. Wickham, E. Scher, A. Kadavanich, A. P. Alivisatos, Shape control of CdSe nanocrystals. *Nature* **404**, 59 (2000).

3. Z. A. Peng, X. Peng, Nearly Monodisperse and Shape-Controlled CdSe Nanocrystals via Alternative Routes: Nucleation and Growth. *Journal of the American Chemical Society* **124**, 3343 (2002/04/01, 2002).

4. L. Manna, E. C. Scher, A. P. Alivisatos, Synthesis of Soluble and Processable Rod,
Arrow-, Teardrop-, and Tetrapod-Shaped CdSe Nanocrystals. *Journal of the American Chemical Society* **122**, 12700 (2000/12/01, 2000).

5. D. V. Talapin, J. H. Nelson, E. V. Shevchenko, S. Aloni, B. Sadtler, A. P. Alivisatos, Seeded Growth of Highly Luminescent CdSe/CdS Nanoheterostructures with Rod and Tetrapod Morphologies. *Nano Letters* **7**, 2951 (2007/10/01, 2007).

6. J. Müller, J. M. Lupton, P. G. Lagoudakis, F. Schindler, R. Koeppe, A. L. Rogach, J. Feldmann, D. V. Talapin, H. Weller, Wave Function Engineering in Elongated Semiconductor Nanocrystals with Heterogeneous Carrier Confinement. *Nano Letters* **5**, 2044 (2005/10/01, 2005).

7. N. N. Hewa-Kasakarage, M. Kirsanova, A. Nemchinov, N. Schmall, P. Z. El-Khoury, A. N. Tarnovsky, M. Zamkov, Radiative Recombination of Spatially Extended Excitons in (ZnSe/CdS)/CdS Heterostructured Nanorods. *Journal of the American Chemical Society* **131**, 1328 (2009/01/28, 2009).

8. J. Müller, J. M. Lupton, A. L. Rogach, J. Feldmann, D. V. Talapin, H. Weller, Monitoring surface charge migration in the spectral dynamics of single CdSe/CdS nanodot/nanorod heterostructures. *Physical Review B* **72**, 205339 (2005).

9. T.-H. Kim, K.-S. Cho, E. K. Lee, S. J. Lee, J. Chae, J. W. Kim, D. H. Kim, J.-Y. Kwon, G. Amaratunga, S. Y. Lee, B. L. Choi, Y. Kuk, J. M. Kim, K. Kim, Full-colour quantum dot displays fabricated by transfer printing. *Nat Photon* **5**, 176 (2011).

10. V. I. Klimov, S. A. Ivanov, J. Nanda, M. Achermann, I. Bezel, J. A. McGuire, A.

Piryatinski, Single-exciton optical gain in semiconductor nanocrystals. *Nature* **447**, 441 (2007).

11. X. Michalet, F. F. Pinaud, L. A. Bentolila, J. M. Tsay, S. Doose, J. J. Li, G. Sundaresan, A. M. Wu, S. S. Gambhir, S. Weiss, Quantum Dots for Live Cells, in Vivo Imaging, and Diagnostics. *Science* **307**, 538 (2005).

12. S. Li, K. Zhang, J.-M. Yang, L. Lin, H. Yang, Single Quantum Dots as Local Temperature Markers. *Nano Letters* 7, 3102 (2007/10/01, 2007).

13. M. J. Ruedas-Rama, E. A. H. Hall, Azamacrocycle Activated Quantum Dot for Zinc Ion Detection. *Analytical Chemistry* **80**, 8260 (2008/11/01, 2008).

14. H. Aouani, S. Itzhakov, D. Gachet, E. s. Devaux, T. W. Ebbesen, H. Rigneault, D. Oron, J. r. m. Wenger, Colloidal Quantum Dots as Probes of Excitation Field Enhancement in Photonic Antennas. *ACS Nano* **4**, 4571 (2010/08/24, 2010).

15. H. Zhu, N. Song, H. Lv, C. L. Hill, T. Lian, Near Unity Quantum Yield of Light-Driven Redox Mediator Reduction and Efficient H2 Generation Using Colloidal Nanorod

Heterostructures. *Journal of the American Chemical Society* **134**, 11701 (2012/07/18, 2012).

16. I. n. Mora-Seró, J. Bisquert, Breakthroughs in the Development of Semiconductor- Sensitized Solar Cells. *The Journal of Physical Chemistry Letters* **1**, 3046 (2010/10/21, 2010).

17. J. B. Delehanty, I. L. Medintz, T. Pons, F. M. Brunel, P. E. Dawson, H. Mattoussi, Self-Assembled Quantum Dot−Peptide Bioconjugates for Selective Intracellular Delivery. *Bioconjugate Chemistry* **17**, 920 (2006/07/01, 2006).

18. P. Pandey, S. P. Singh, S. K. Arya, V. Gupta, M. Datta, S. Singh, B. D. Malhotra, Application of thiolated gold nanoparticles for the enhancement of glucose oxidase activity. Langmuir 23, 3333–3337 (2007).

19. G. Tikhomirov, S. Hoogland, P. E. Lee, A. Fischer, E. H. Sargent, S. O. Kelley, DNAbased programming of quantum dot valency, self-assembly and luminescence. *Nat Nano* **6**, 485 (2011).

20. I. L. Medintz, H. T. Uyeda, E. R. Goldman, H. Mattoussi, Quantum dot bioconjugates for imaging, labelling and sensing. *Nat Mater* **4**, 435 (2005).

21. I. L. Medintz, M. H. Stewart, S. A. Trammell, K. Susumu, J. B. Delehanty, B. C. Mei, J. S. Melinger, J. B. Blanco-Canosa, P. E. Dawson, H. Mattoussi, Quantum-dot/dopamine bioconjugates function as redox coupled assemblies for in vitro and intracellular pH sensing. *Nature Materials* **9**, 676 (2010).

22. J. Xu, T. Teslaa, T.-H. Wu, P.-Y. Chiou, M. A. Teitell, S. Weiss, Nanoblade Delivery and Incorporation of Quantum Dot Conjugates into Tubulin Networks in Live Cells. *Nano Letters* **12**, 5669 (2012/11/14, 2012).

23. M. L. Schipper, G. Iyer, A. L. Koh, Z. Cheng, Y. Ebenstein, A. Aharoni, S. Keren, L. A. Bentolila, J. Q. Li, J. H. Rao, X. Y. Chen, U. Banin, A. M. Wu, R. Sinclair, S. Weiss, S. S. Gambhir, Particle Size, Surface Coating, and PEGylation Influence the Biodistribution of Quantum Dots in Living Mice. *Small* **5**, 126 (Jan, 2009). *Science Advances*

24. J. B. Blanco-Canosa, M. Wu, K. Susumu, E. Petryayeva, T. L. Jennings, P. E. Dawson, W. R. Algar, I. L. Medintz, Recent progress in the bioconjugation of quantum dots.
Coordination Chemistry Reviews **263–264**, 101 (2014).

25. W. T. Al-Jamal, K. T. Al-Jamal, B. Tian, L. Lacerda, P. H. Bomans, P. M. Frederik, K. Kostarelos, Lipid−Quantum Dot Bilayer Vesicles Enhance Tumor Cell Uptake and Retention in Vitro and in Vivo. *ACS Nano* **2**, 408 (2008/03/01, 2008).

26. J. A. Kloepfer, N. Cohen, J. L. Nadeau, FRET between CdSe Quantum Dots in Lipid Vesicles and Water- and Lipid-soluble Dyes. *The Journal of Physical Chemistry B* **108**,
17042 (2004/11/01, 2004).

27. G. Gopalakrishnan, C. Danelon, P. Izewska, M. Prummer, P.-Y. Bolinger, I. Geissbühler, D. Demurtas, J. Dubochet, H. Vogel, Multifunctional Lipid/Quantum Dot Hybrid Nanocontainers for Controlled Targeting of Live Cells. *Angewandte Chemie International Edition* **45**, 5478 (2006).

28. H. S. Wi, S. J. Kim, K. Lee, S. M. Kim, H. S. Yang, H. K. Pak, Incorporation of quantum dots into the lipid bilayer of giant unilamellar vesicles and its stability. *Colloids and*
Surfaces B: Biointerfaces **97**, 37 (2012).

29. M. Langecker, V. Arnaut, T. G. Martin, J. List, S. Renner, M. Mayer, H. Dietz, F. C. Simmel, Synthetic Lipid Membrane Channels Formed by Designed DNA Nanostructures.
Science **338**, 932 (2012).

30. A. Seifert, K. Göpfrich, J. R. Burns, N. Fertig, U. F. Keyser, S. Howorka, Bilayer-Spanning DNA Nanopores with Voltage-Switching between Open and Closed State. *ACS*

Nano **9**, 1117 (2015/02/24, 2015).

31. J. Geng, K. Kim, J. Zhang, A. Escalada, R. Tunuguntla, L. R. Comolli, F. I. Allen, A. V. Shnyrova, K. R. Cho, D. Munoz, Y. M. Wang, C. P. Grigoropoulos, C. M. Ajo-Franklin, V. A. Frolov, A. Noy, Stochastic transport through carbon nanotubes in lipid bilayers and live cell membranes. *Nature* **514**, 612 (2014).

32. K. Becker, J. M. Lupton, J. Muller, A. L. Rogach, D. V. Talapin, H. Weller, J. Feldmann, Electrical control of Forster energy transfer. *Nat Mater* **5**, 777 (2006).

33. R. M. Kraus, P. G. Lagoudakis, A. L. Rogach, D. V. Talapin, H. Weller, J. M. Lupton, J. Feldmann, Room-Temperature Exciton Storage in Elongated Semiconductor Nanocrystals. *Physical Review Letters* **98**, 017401 (2007).

34. K. Park, Z. Deutsch, J. J. Li, D. Oron, S. Weiss, Single Molecule Quantum-Confined Stark Effect Measurements of Semiconductor Nanoparticles at Room Temperature. *ACS Nano* **6**, 10013 (2012/11/27, 2012).

35. J. D. Marshall, M. J. Schnitzer, Optical Strategies for Sensing Neuronal Voltage Using Quantum Dots and Other Semiconductor Nanocrystals. *ACS Nano* 7, 4601 (2013/05/28, 2013).

36. J. M. Kralj, A. D. Douglass, D. R. Hochbaum, D. Maclaurin, A. E. Cohen, Optical recording of action potentials in mammalian neurons using a microbial rhodopsin. Nat. Methods 9, 90–95 (2012).

37. E. W. Miller, J. Y. Lin, E. P. Frady, P. A. Steinbach, W. B. Kristan Jr., R. Y. Tsien, Optically monitoring voltage in neurons by photo-induced electron transfer through molecular wires. Proc. Natl. Acad. Sci. U.S.A. 109, 2114–2119 (2012).

38. K. Park, S. Weiss, Design rules for membrane-embedded voltage-sensing nanoparticles. Biophys. J. 112, 703–713 (2017).

39. F. Pinaud, D. King, H.-P. Moore, S. Weiss, Bioactivation and Cell Targeting of

Semiconductor CdSe/ZnS Nanocrystals with Phytochelatin-Related Peptides. *Journal of the American Chemical Society* **126**, 6115 (2004/05/01, 2004).

40. F. Pinaud, X. Michalet, L. A. Bentolila, J. M. Tsay, S. Doose, J. J. Li, G. Iyer, S. Weiss, Advances in fluorescence imaging with quantum dot bio-probes. *Biomaterials* **27**, 1679 (2006). *Science Advances* Manuscript Template Page **57** of **58**

41. J. M. Tsay, S. Doose, F. Pinaud, S. Weiss, Enhancing the photoluminescence of peptidecoated nanocrystals with shell composition and UV irradiation. *Journal of Physical*
Chemistry B **109**, 1669 (Feb 10, 2005).

42. G. Iyer, F. Pinaud, J. Tsay, S. Weiss, Solubilization of Quantum Dots with a Recombinant Peptide from Escherichia coli. *Small* **3**, 793 (2007).

43. G. Iyer, X. Michalet, Y.-P. Chang, F. F. Pinaud, S. E. Matyas, G. Payne, S. Weiss, High Affinity scFv–Hapten Pair as a Tool for Quantum Dot Labeling and Tracking of Single
Proteins in Live Cells. *Nano Letters* **8**, 4618 (2008/12/10, 2008).

44. A. Senes, D. C. Chadi, P. B. Law, R. F. S. Walters, V. Nanda, W. F. Degrado, E(z), a depth-dependent potential for assessing the energies of insertion of amino acid side-chains into membranes: derivation and applications to determining the orientation of transmembrane and interfacial helices. *J Mol Biol* **366**, 436 (2007/02//, 2007).

45. I. Wrobel, D. Collins, Fusion of cationic liposomes with mammalian cells occurs after endocytosis. *Biochimica et Biophysica Acta (BBA) - Biomembranes* **1235**, 296 (1995).

46. D. Axelrod, Carbocyanine dye orientation in red cell membrane studied by microscopic fluorescence polarization. *Biophysical Journal* **26**, 557 (1979).

47. J. Xu, P. Ruchala, Y. Ebenstain, J. J. Li, S. Weiss, Stable, Compact, Bright Biofunctional Quantum Dots with Improved Peptide Coating. *The Journal of Physical Chemistry B* **116**, 11370 (2012/09/13, 2012).

48. C. Lonez, M. Lensink, E. Kleiren, J.-M. Vanderwinden, J.-M. Ruysschaert, M. Vandenbranden, Fusogenic activity of cationic lipids and lipid shape distribution. *Cellular and Molecular Life Sciences* **67**, 483 (2010/02/01, 2010).

49. J. Park, C. A. Werley, V. Venkatachalam, J. M. Kralj, S. D. Dib-Hajj, S. G. Waxman, A. E. Cohen, Screening Fluorescent Voltage Indicators with Spontaneously Spiking HEK Cells. *PloS One* **8**, e85221 (2013).

50. M. Nirmal, B. O. Dabbousi, M. G. Bawendi, J. J. Macklin, J. K. Trautman, T. D. Harris, L. E. Brus, Fluorescence intermittency in single cadmium selenide nanocrystals. *Nature* **383**, 802 (1996).

51. D. V. Talapin, R. Koeppe, S. Götzinger, A. Kornowski, J. M. Lupton, A. L. Rogach, O. Benson, J. Feldmann, H. Weller, Highly Emissive Colloidal CdSe/CdS Heterostructures of Mixed Dimensionality. *Nano Letters* **3**, 1677 (2003/12/01, 2003).

52. J. I. Climente, J. L. Movilla, J. Planelles, Auger Recombination Suppression in Nanocrystals with Asymmetric Electron–Hole Confinement. *Small* **8**, 754 (2012).

53. K. Kinosita, H. Itoh, S. Ishiwata, K. Hirano, T. Nishizaka, T. Hayakawa, Dual-view microscopy with a single camera: real-time imaging of molecular orientations and calcium. *The Journal of Cell Biology* **115**, 67 (1991).

54. E. Molokanova, Bartel, J.A., Zhao, W., Naasani, I., Ignatius, M.J., Treadway, J.A., Savtchenko, A., Quantum dots move beyond fluorescence imaging. *Biophotonics Int.*, 26 (2008).

55. M. Molokanova, A. Savchenko, Bright future of optical assays for ion channel drug discovery. *Drug Discovery Today* **13**, 14 (Jan, 2008).

56. H. Shen, Interactive notebooks: Sharing the code. *Nature* **515**, (Nov., 2014).

57. Membrane insertion of- and membrane potential sensing by-semiconductor voltage nanosensors: feasibility demonstration, by Kyoungwon Park, Yung Kuo, Volodymyr Shvadchak, Antonino Ingargiola, Xinghong Dai, Lawrence Hsiung, Wookyeom Kim, Z. Hong Zhou, Peng Zou, Alex J. Levine, Jack Li, and Shimon Weiss., bioRxiv preprint available at http://dx.doi.org/10.1101/044057.

58. Design Rules for Membrane-Embedded Voltage-Sensing Nanoparticles, by Kyoungwon Park and Shimon Weiss, Biophysical Journal 112, 703–713, February 28, 2017.

59. Single Molecule Quantum-Confined Stark Effect Measurements of Semiconductor Nanoparticles at Room Temperature, by KyoungWon Park, Zvicka Deutsch, J. Jack Li, Dan Oron, and Shimon Weiss, published on line 10.1021/nn303719m.

60. https://www.hamamatsu.com/jp/en/A12801-01.html.

61. http://dx.doi.org/10.6084/m9.figshare.1445980, dataset 122018_take1 100Hz.zip

62. https://figshare.com/articles/zqd_tif/4229531. The analysis code is published in a public github repository : https://github.com/pkw0818/spiking-cell-analysis.

63. Park et al., Sci. Adv. 2018;4: e1601453 and supporting information. February 2018.

Conclusion

This concludes the description of the preferred embodiment of the present invention. The foregoing description of one or more embodiments of the invention has been presented for the purposes of illustration and description. It is not intended to be exhaustive or to limit the invention to the precise form disclosed. Many modifications and variations are possible in light of the above teaching. It is intended that the scope of the invention be limited not by this detailed description, but rather by the claims appended hereto.

CLAIMS:

1. A composition of matter, comprising:

peptides attached to a semiconductor nanorod, wherein:

the peptides each comprise a hydrophilic segment connected to a lipophilic segment, the lipophilic segment and the hydrophilic segment comprising cysteine residues,

the hydrophilic segment attaches to an end of the semiconductor nanorod,

the lipophilic segment attaches to a side of the semiconductor nanorod, and

the cysteine residues mediate attachment of the peptides to the semiconductor nanorod.

2. The composition of matter of claim 1, wherein the peptides each comprise the lipophilic segment terminated by a fatty acid.

3. The composition of matter of any of the preceding claims, wherein the liphophilic segment comprises an alpha-helix structure.

4. The composition of matter of claim 3, wherein the cysteine residues are disposed in the alpha-helix structure so that a side of the alpha-helix structure facing the semiconductor nanorod is cysteine rich and a side of the alpha-helix structure facing an exterior is lipophilic.

5. The composition of matter of any of the preceding claims, wherein the hydrophilic segment comprises a flexible unstructured domain (non-helical structure) that bends around the end.

6. The composition of matter of any of the preceding claims, wherein the peptides each comprise residues that preferentially localize at a membrane-water interface

7. The composition of matter of any of the preceding claims, wherein each of the peptides further comprise a segment of aliphatic amino acids that prevent aggregation of the peptides in solution.

8. The composition of matter of claim 7, wherein the aliphatic amino acids comprise a hydroxyl-containing Thr residue and an acidic residue.

9. The composition of matter of any of the preceding claims, wherein a sequence of each of the peptides is Myristoyl- CLTCALTCMECTLKCWYKRGCRGCG-COOH (SEQ ID NO:1).

10. The composition of matter of any of the preceding claims, wherein:

the peptides comprise between 2 and 20 peptide chains disposed around the nanorod,

the hydrophilic segment comprises less cysteine residues as compared to the lipophilic segment, and

each peptide extends over at least half the length of the nanorod.

11. The composition of matter of any of the preceding claims, wherein the semiconductor nanorod has a length in a range of 5 – 50 nm and a width in a range of 1-10 nm.

12. The composition of matter of any of the preceding claims inserted into a cell membrane, wherein the semiconductor nanorod has a length longer than a thickness of the cell membrane.

13. The composition of matter of claim 12, wherein the cell membrane is a lipid bilayer.

14. The composition of matter of any of the preceding claims, wherein the semiconductor nanorod comprises at least one material selected from CdSe and ZnSe-CdS.

15. The composition of matter of any of the preceding claims, wherein the semiconductor nanoparticle comprises a semiconductor having a type II band offset.

16. The composition of matter of any of the preceding claims, wherein the semiconductor nanorod has a bandgap in a range of 0.6 eV - 1.77 eV.

17. A composition of matter, comprising:

peptides attached to a semiconductor nanorod, wherein the peptides each comprise a helical and a flexible part binding different faces of the nanorod.

18. An apparatus for measuring a membrane potential, comprising:

a camera measuring one or more changes in fluorescence emitted from one or more peptide coated nanorods inserted in a cell membrane when the nanorods are excited with electromagnetic radiation, wherein:

the one or more changes include a response to one or more membrane potentials applied to the one or more nanorods by the cell membrane, the one or more nanorods each have a long axis substantially parallel to the cell membrane's normal, and

the one or more nanorods each protrude from both sides of the cell membrane; and

a computer coupled to the camera, wherein the computer:

filters the fluorescence so as to extract the response from noise, and

determines one or more magnitudes and/or one or more waveforms of the membrane potentials from the response.

19. The apparatus of claim 18, wherein:

the camera measures the fluorescence comprising a wavelength shift in response to the membrane potentials, and

the computer determines the one or more magnitudes and/or one or more waveforms by modeling the wavelength shift as a Quantum Confined Stark Effect.

20. The apparatus of any of the claims 18-19, further comprising a source of the electromagnetic radiation comprising blue and/or ultraviolet (UV) electromagnetic radiation (a wavelength in a range of 350 nm – 1 micron), wherein the nanorods:

emit the fluorescence in response to being excited with the electromagnetic radiation when the membrane potentials are being applied to the nanorods.

21. The apparatus of any of the claims 18-20, wherein the camera measures the fluorescence with an acquisition rate of more than 1 Hz -5 kHz.

22. The apparatus of any of the claims claim 18-21, wherein the camera comprises an electronic imaging sensor detecting the fluorescence.

23. The apparatus of any of the claims 18-22, wherein the computer determines the one or more magnitudes and/or waveforms of the membrane potentials from the fluorescence emitted from a single nanorod.

24. The apparatus of any of the claims 18-22, wherein the nanorods comprise the composition of matter of any of the claims 1-17.

25. A method of measuring a membrane potential, comprising:

filtering fluorescence so as to extract one or more signals from noise, wherein:

the one or more signals correspond to one or more changes in the fluorescence emitted from one or more peptide coated nanorods inserted in a cell membrane,

the one or more changes are in response to one or more membrane potentials applied to the one or more nanorods by the cell membrane,

the one or more nanorods each have a long axis substantially parallel to the cell membrane's normal, and the one or more nanorods each protrude from both sides of the cell membrane; and

determining one or more magnitudes and/or one or more waveforms of the membrane potentials from the one or more signals.

26. The method of any of claim 25, further comprising:

obtaining a fluorescence image of the nanorods inserted in the cell membrane; and

processing the image so as to identify the signal comprising a single diffraction limited fluorescence spot.

27. The method of claim 26, wherein the fluorescence spot corresponds to fluorescence from a single nanorod.

28. The method of any of the claims 25-27, further comprising disposing the nanorods on a cell membrane so that the nanorods self assemble and insert into the cell membrane.

29. The method of any of the claims 25-28, wherein the cell membrane is a lipid bilayer.

30. The method of any of the claims 25-29, wherein the nanorods comprise the composition of matter of any of the claims 1-17.

31. An apparatus for measuring a membrane potential, comprising:

a detector measuring a change in electromagnetic radiation emitted from one or more nanorods inserted in a cell membrane, wherein:

the change comprises a response to one or more membrane potentials applied to the one or more nanorods by the cell membrane,

the one or more nanorods each have a long axis substantially parallel to the cell membrane's normal,

the one or more nanorods each protrude from both sides of the cell membrane, and

the nanorods comprise the composition of matter of any of the claims 1-16; and

a computer coupled to the detector, wherein the computer:

filters the change so as to extract the response from noise, and

determines one or more magnitudes and/or one or more waveforms of the membrane potentials from the response.

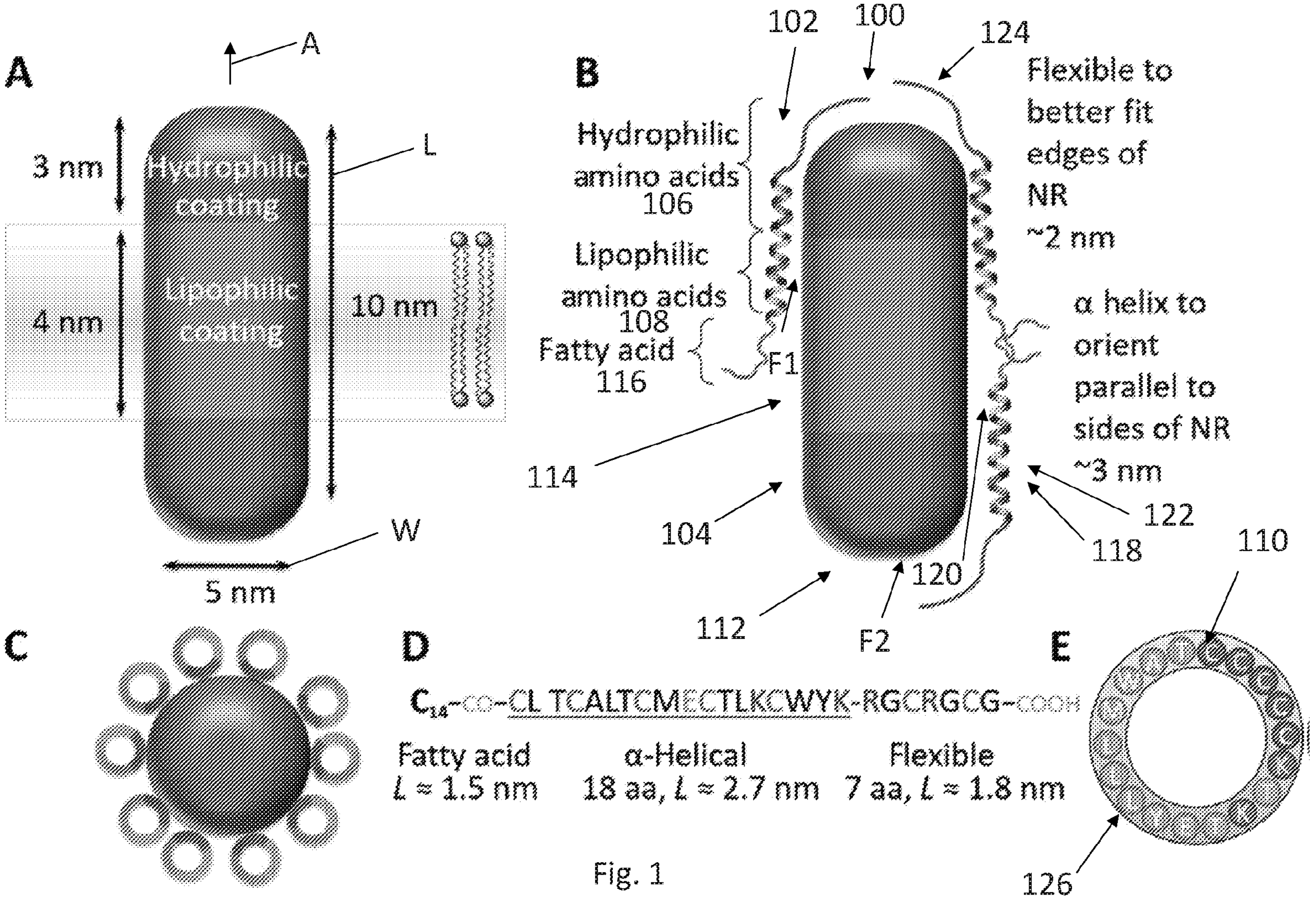
A
A
3 nm
4 nm
Hydrophilic coating
Lipophilic coating
L
10 nm
W
5 nm
B
102
100
124
Hydrophilic amino acids 106
Lipophilic amino acids 108
Fatty acid 116
F1
114
104
112
F2
120
118
122
Flexible to better fit edges of NR ~2 nm
α helix to orient parallel to sides of NR ~3 nm
C
D
C_{14}~CO~CL TCALTCMECTLKCWYK-RGCRGCG~COOH
Fatty acid L ≈ 1.5 nm
α-Helical 18 aa, L ≈ 2.7 nm
Flexible 7 aa, L ≈ 1.8 nm
E
110
126

Fig. 1

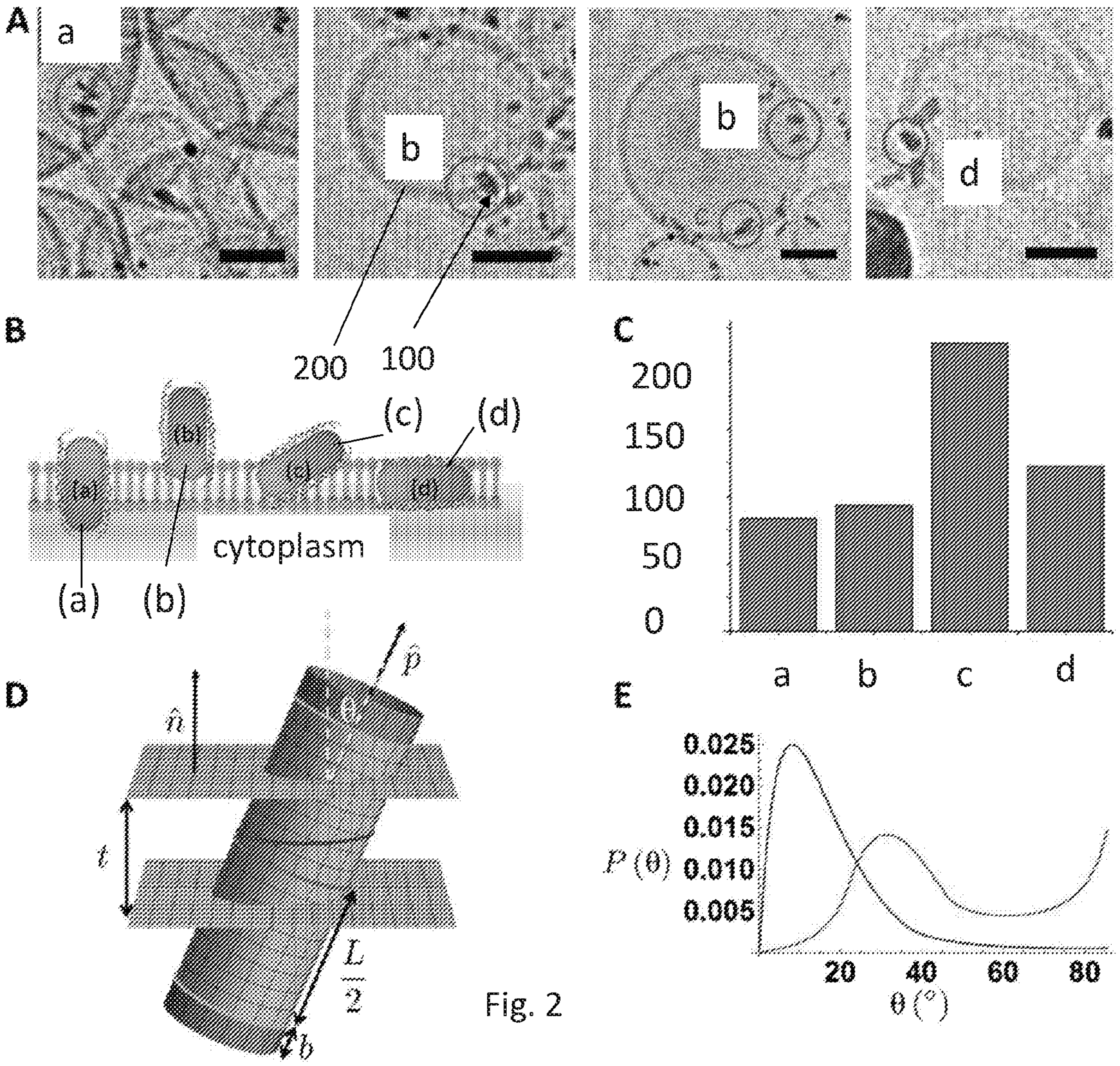
A
a
b
b
d
B
200
100
(a)
(b)
(c)
(d)
cytoplasm
C
200
150
100
50
0
a
b
c
d
D
$\hat{p}$
$\hat{n}$
θ
t
$\frac{L}{2}$
b
E
0.025
0.020
0.015
0.010
0.005
$P(\theta)$
20
40
60
80
$\theta(°)$

Fig. 2

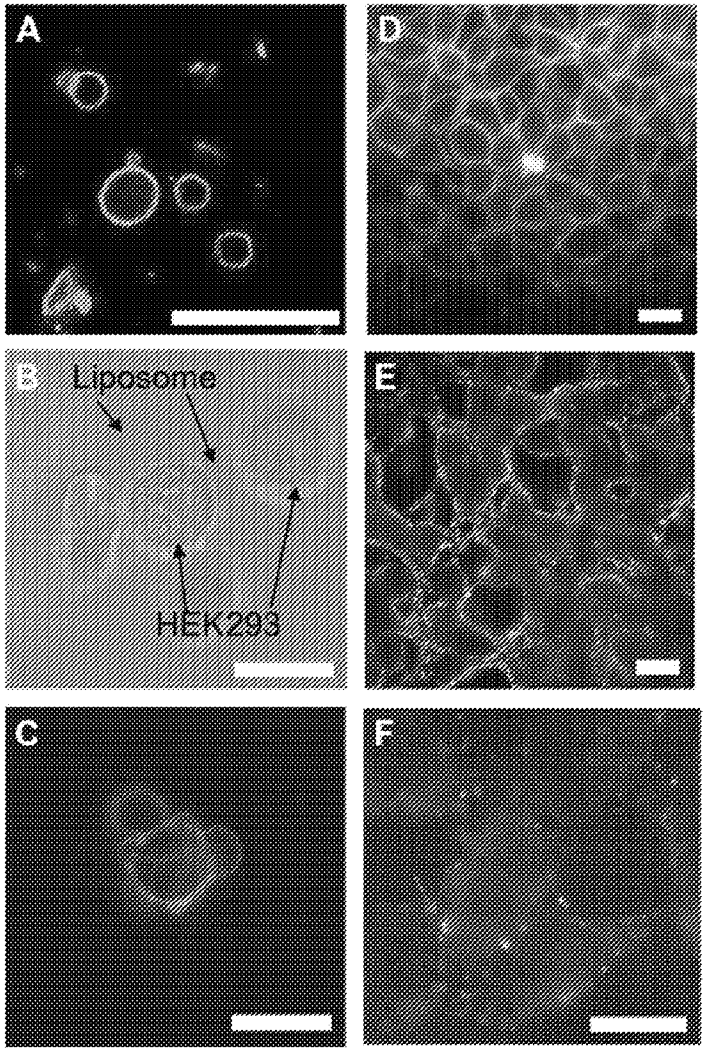

Fig. 3

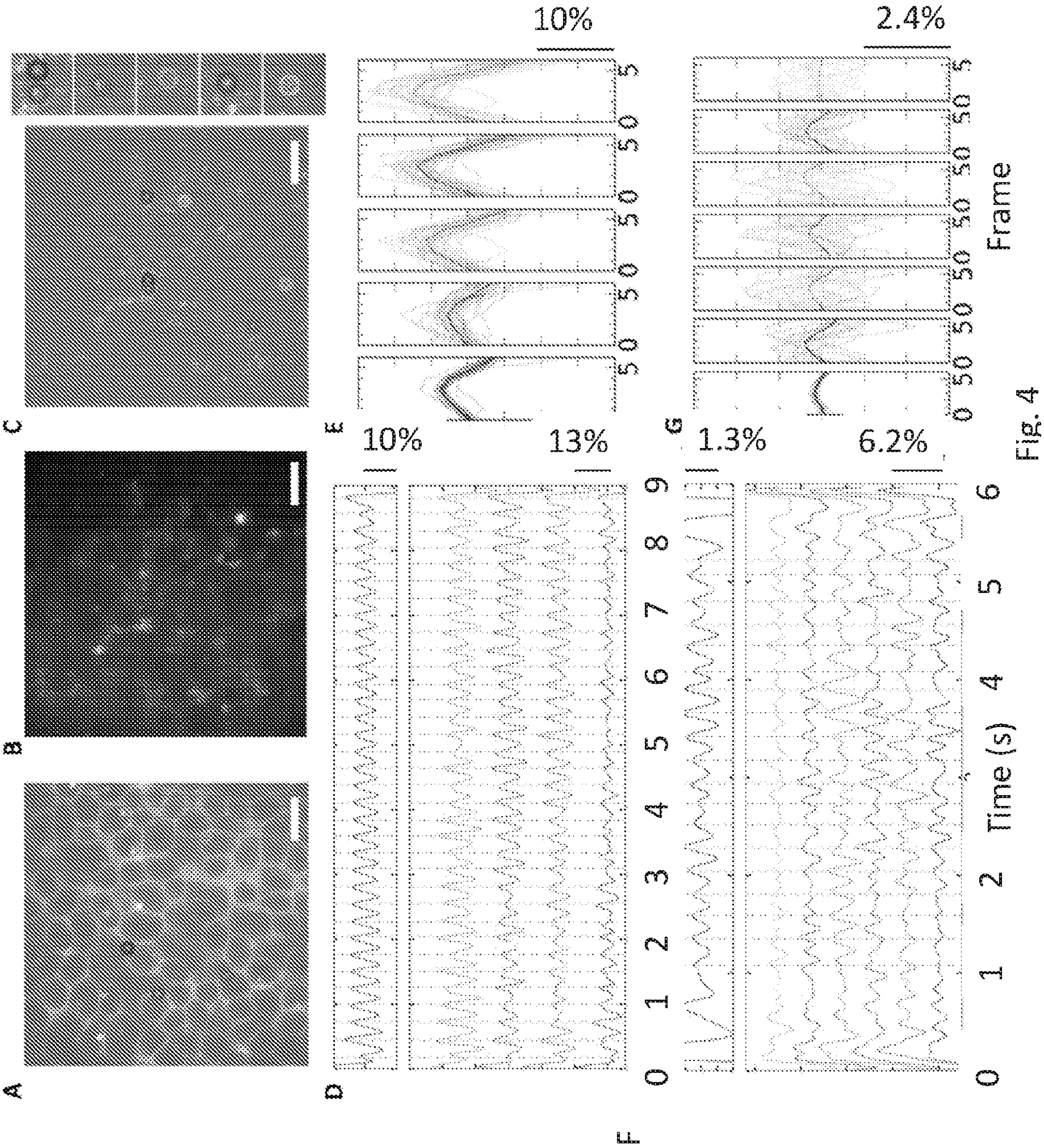

Fig. 4

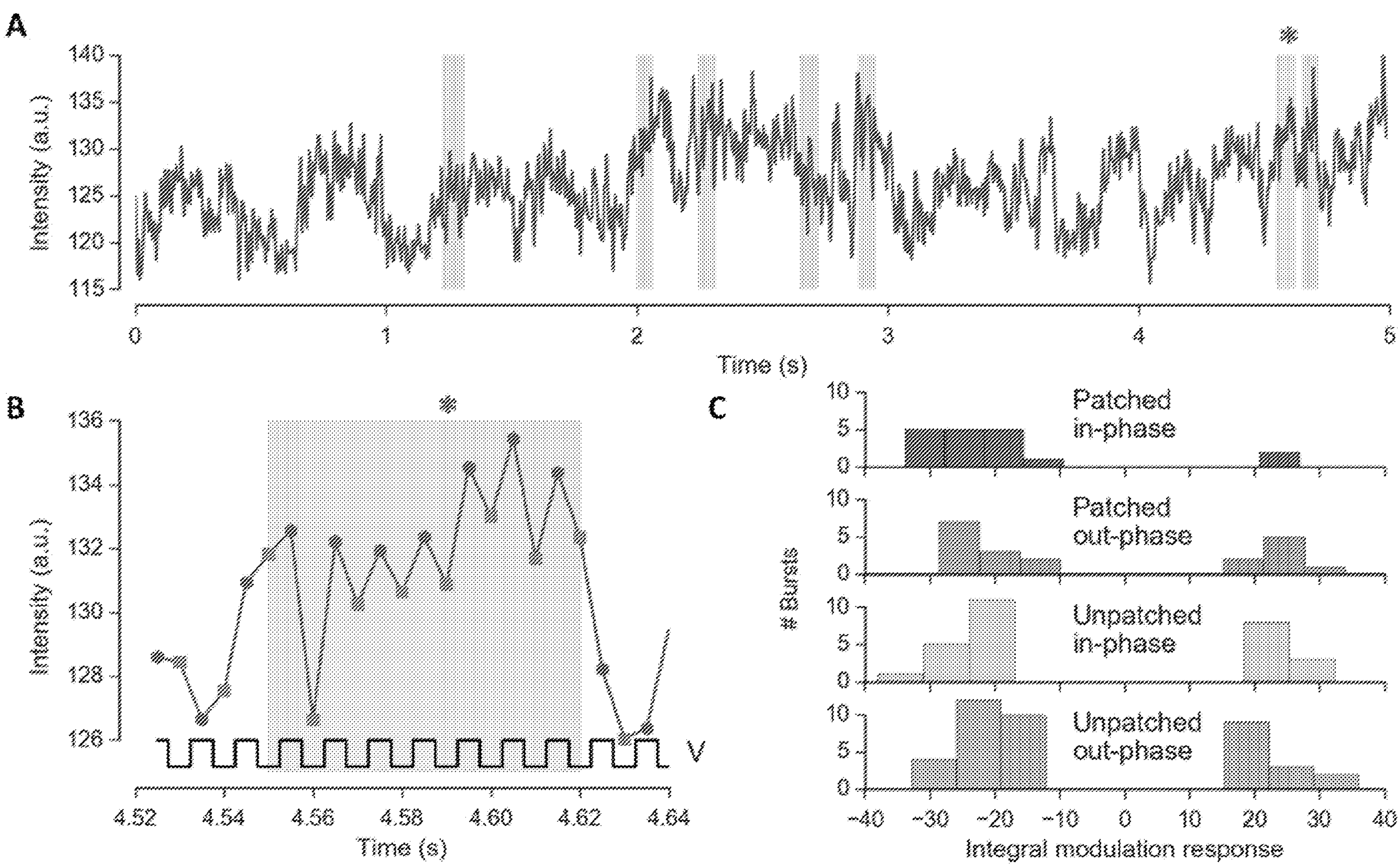
A
Intensity (a.u.)
140
135
130
125
120
115
*
0
1
2
3
4
5
Time (s)
B
Intensity (a.u.)
136
134
132
130
128
126
*
V
4.52
4.54
4.56
4.58
4.60
4.62
4.64
Time (s)
C
Bursts
10
5
0
Patched
in-phase
Patched
out-phase
Unpatched
in-phase
Unpatched
out-phase
−40
−30
−20
−10
0
10
20
30
40
Integral modulation response

Fig. 5

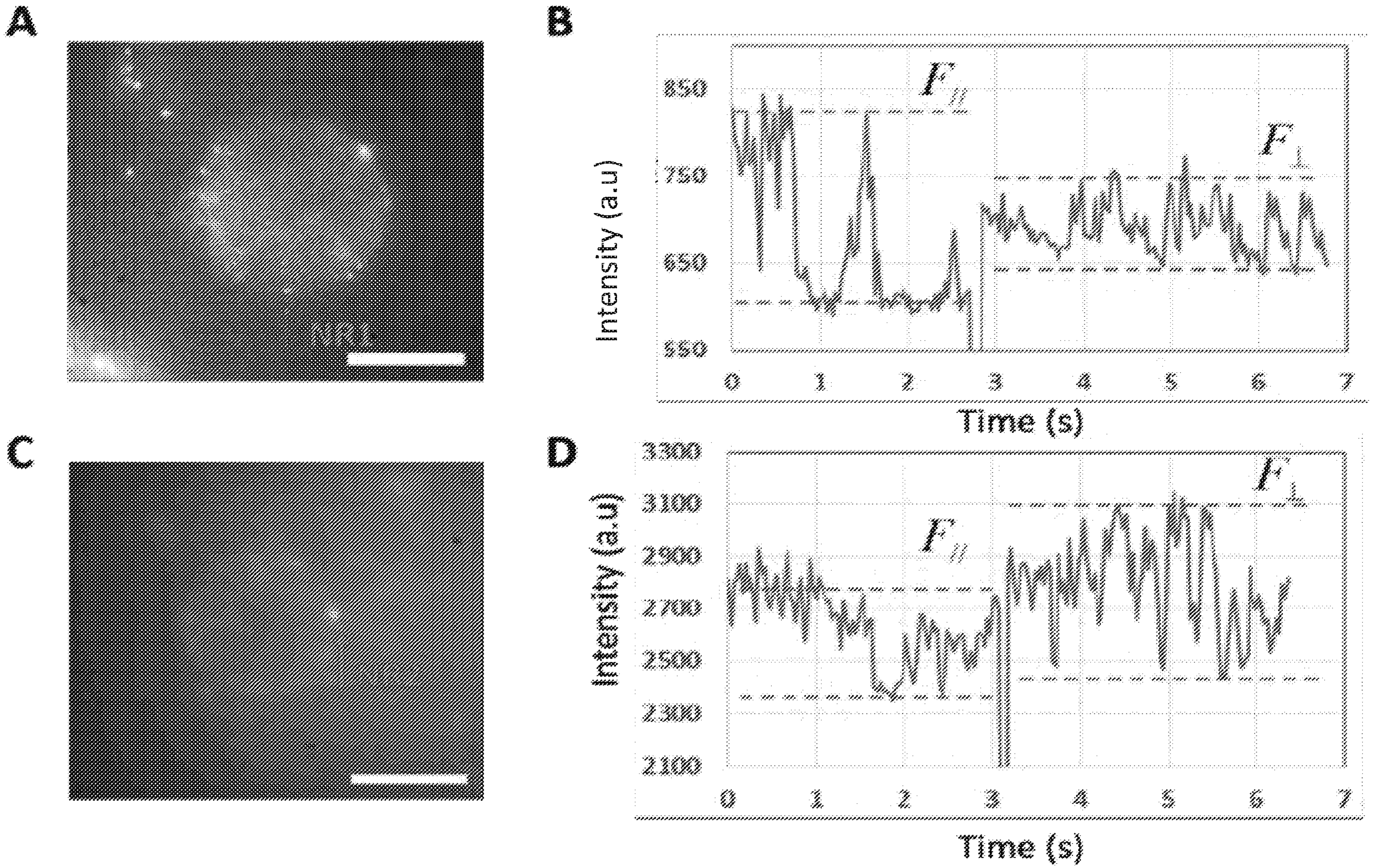
A
B
C
D
850
750
650
550
Intensity (a.u)
0
1
2
3
4
5
6
7
Time (s)
$F_{//}$
$F_{\perp}$
3300
3100
2900
2700
2500
2300
2100

Fig. 6

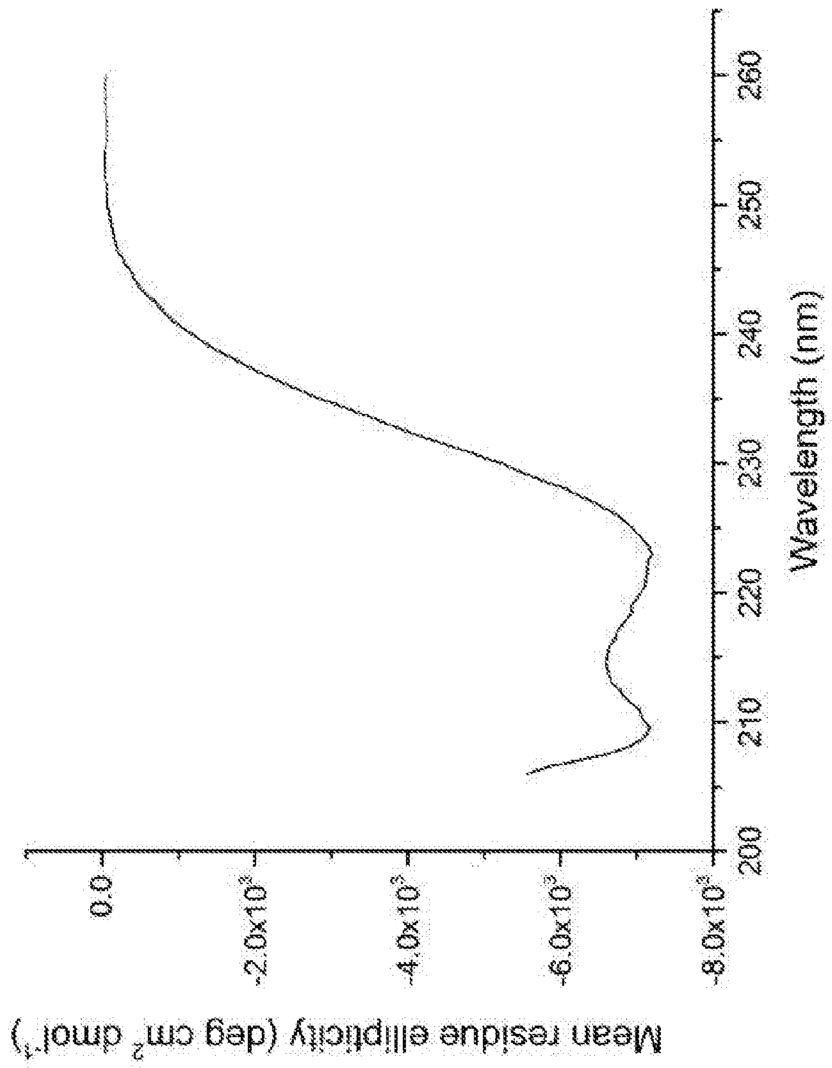
Mean residue ellipticity (deg cm^2 dmol^{-1})
0.0
-2.0x10^3
-4.0x10^3
-6.0x10^3
-8.0x10^3
200
210
220
230
240
250
260
Wavelength (nm)

Fig. 7

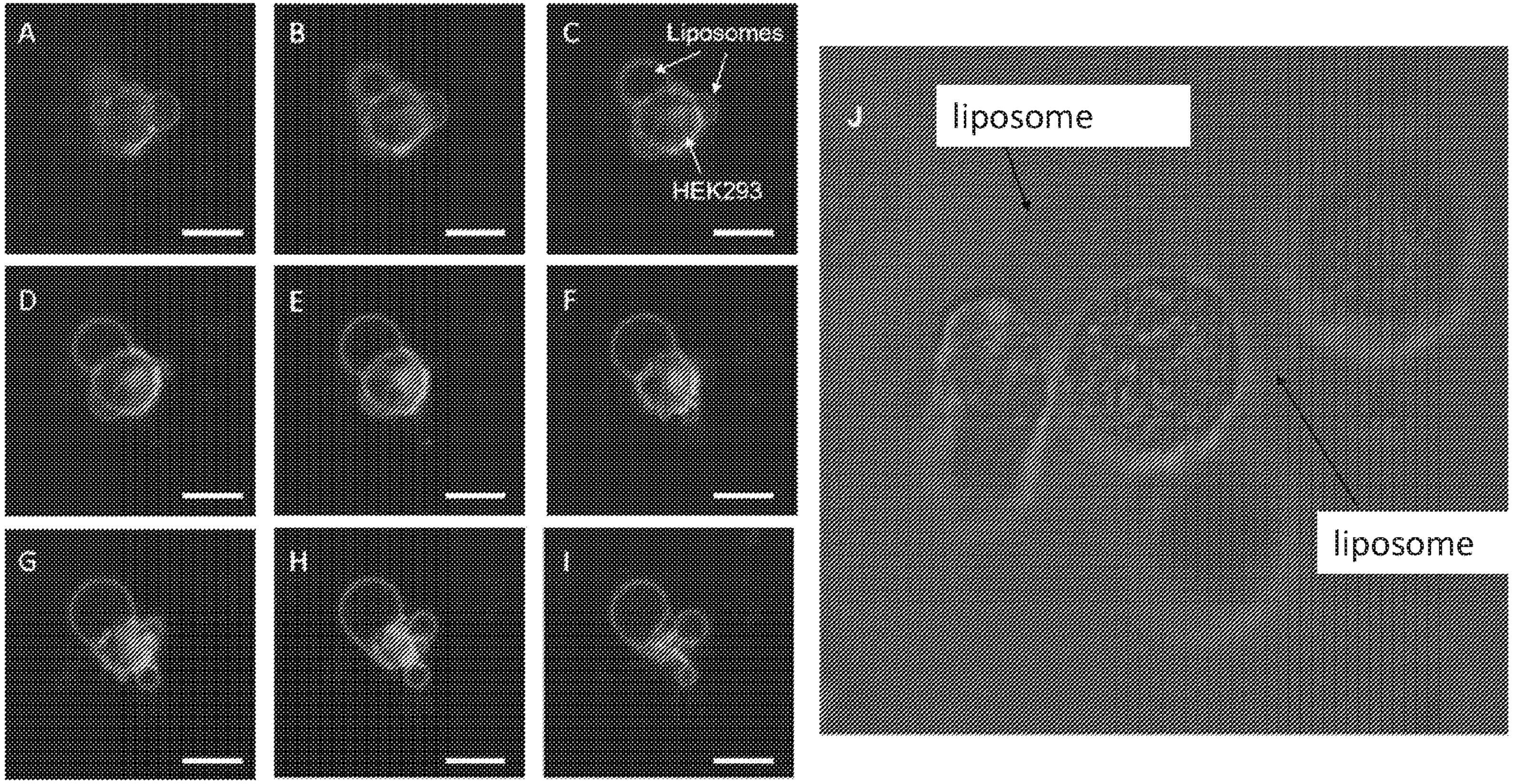

Fig. 8

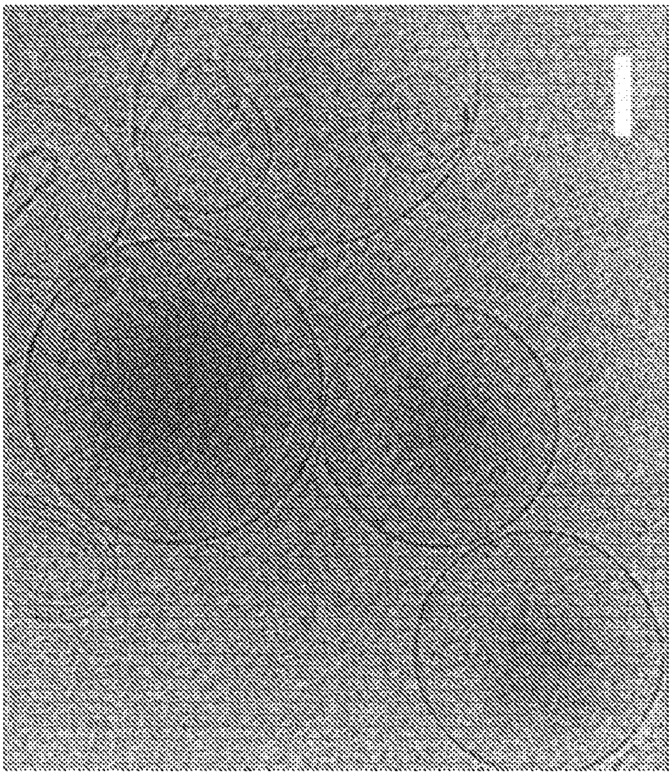

Fig. 9

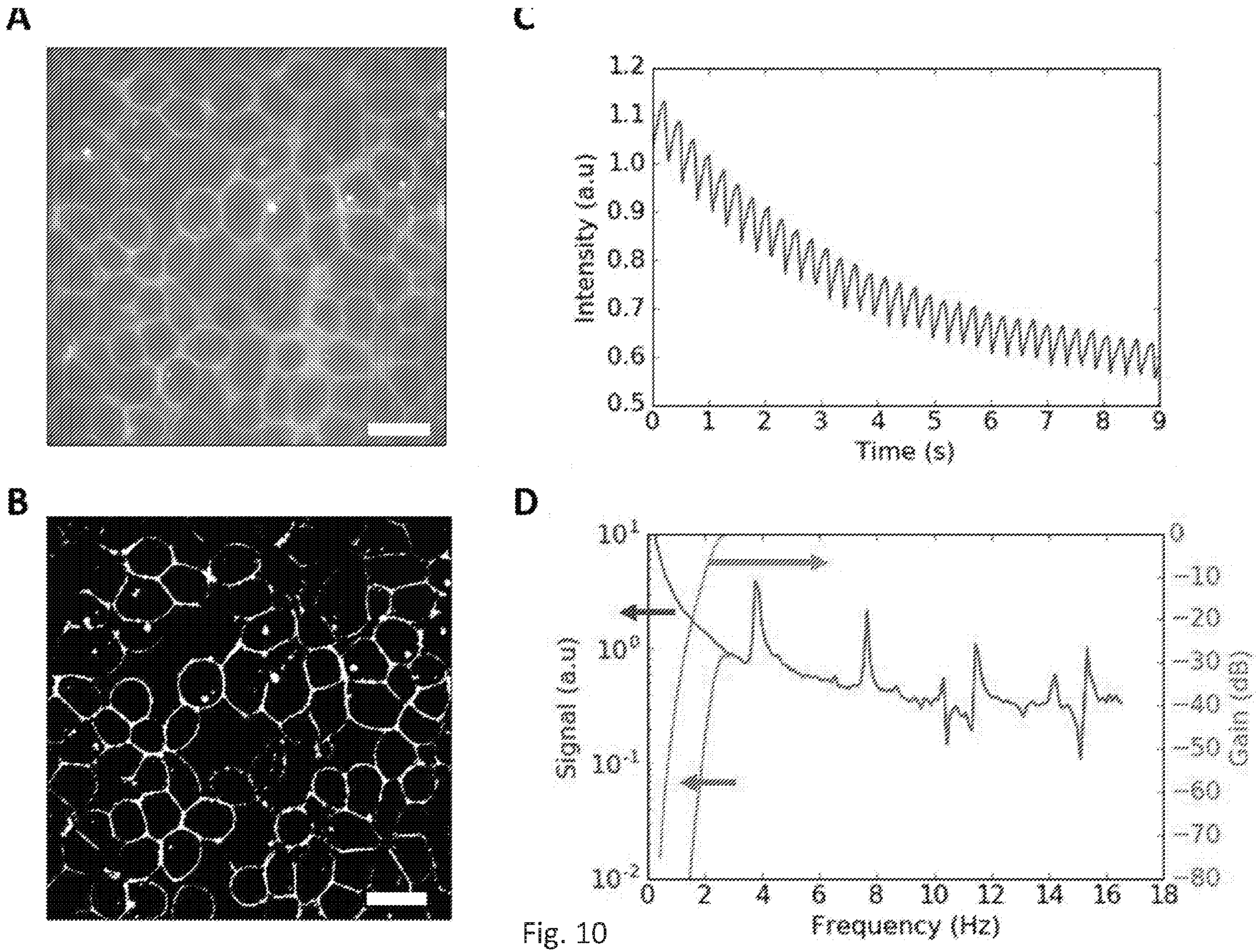
A
B
C
1.2
1.1
1.0
0.9
0.8
0.7
0.6
0.5
Intensity (a.u)
0
1
2
3
4
5
6
7
8
9
Time (s)
D
10^1
10^0
10^{-1}
10^{-2}
Signal (a.u)
0
−10
−20
−30
−40
−50
−60
−70
−80
Gain (dB)
0
2
4
6
8
10
12
14
16
18
Frequency (Hz)

Fig. 10

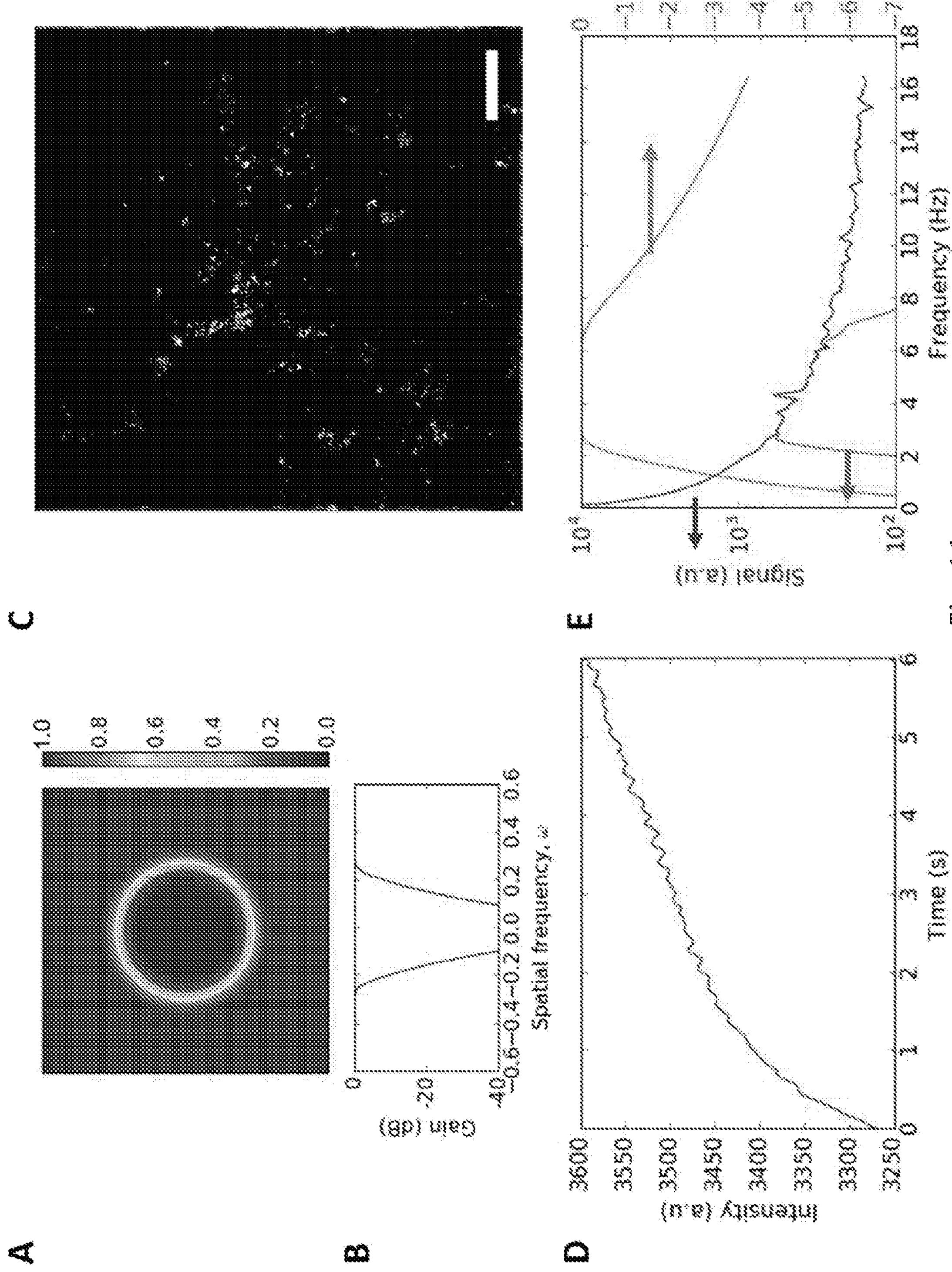
A
1.0
0.8
0.6
0.4
0.2
0.0
B
Gain (dB)
0
-20
-40
−0.6
−0.4
−0.2
0.0
0.2
0.4
0.6
Spatial frequency, ω
C
D
Intensity (a.u)
3600
3550
3500
3450
3400
3350
3300
3250
0
1
2
3
4
5
6
Time (s)
E
Signal (a.u)
10^4
10^3
10^2
0
2
4
6
8
10
12
14
16
18
Frequency (Hz)
Gain (dB)
0
−10
−20
−30
−40
−50
−60
−70

Fig. 11

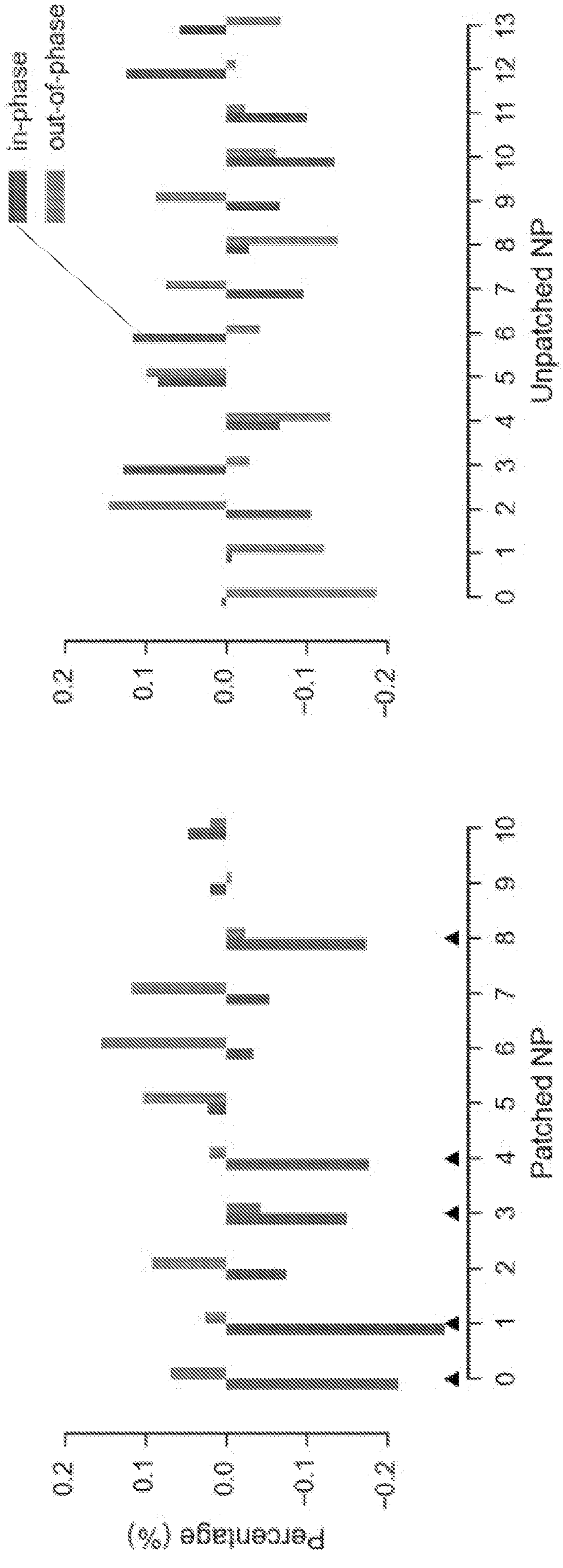
Percentage (%)
0.2
0.1
0.0
−0.1
−0.2
0
1
2
3
4
5
6
7
8
9
10
Patched NP
in-phase
out-of-phase
0
1
2
3
4
5
6
7
8
9
10
11
12
13
Unpatched NP

Fig. 12

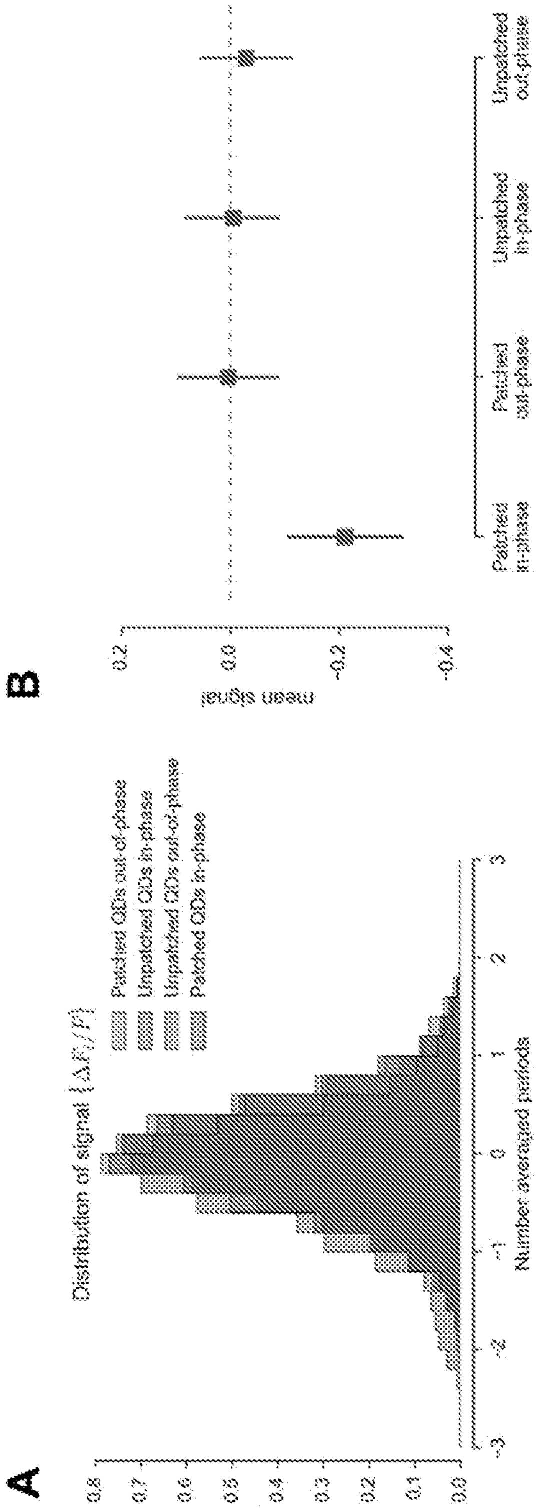
A
Distribution of signal ($\Delta F_i/F$)
▨ Patched QDs out-of-phase
▨ Unpatched QDs in-phase
▨ Unpatched QDs out-of-phase
▨ Patched QDs in-phase
mean signal
0.8
0.7
0.6
0.5
0.4
0.3
0.2
0.1
0.0
-3
-2
-1
0
1
2
3
Number averaged periods
B
mean signal
0.2
0.0
-0.2
-0.4
Patched in-phase
Patched out-phase
Unpatched in-phase
Unpatched out-phase

Fig. 13

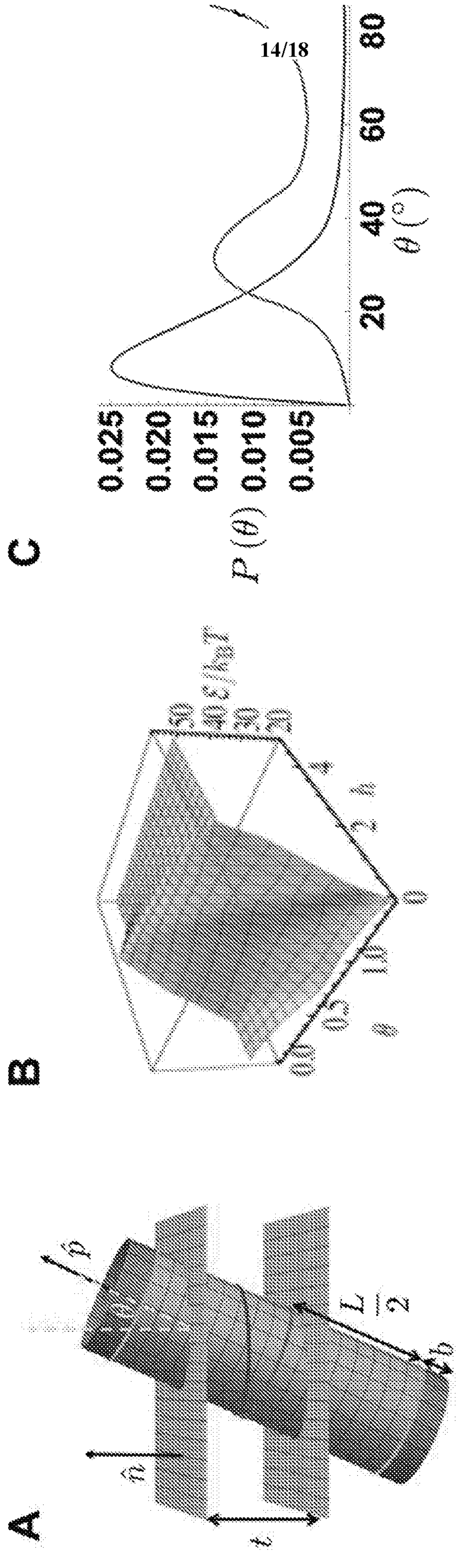
A
$\hat{n}$
$\hat{p}$
t
$\frac{L}{2}$
b
B
E/k_BT
50
40
30
20
0
2
4
h
0.0
0.5
1.0
θ
C
$P(\theta)$
0.025
0.020
0.015
0.010
0.005
20
40
60
80
$\theta(°)$

Fig. 14

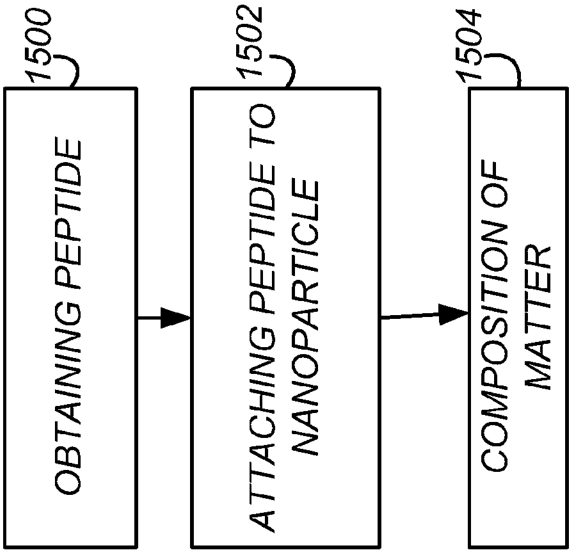
1500
OBTAINING PEPTIDE
1502
ATTACHING PEPTIDE TO NANOPARTICLE
1504
COMPOSITION OF MATTER

Fig. 15

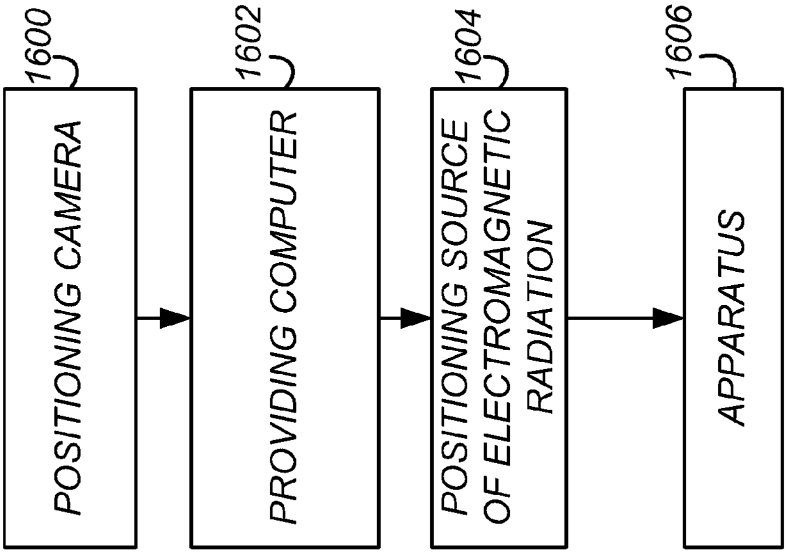
1600
POSITIONING CAMERA
1602
PROVIDING COMPUTER
1604
POSITIONING SOURCE OF ELECTROMAGNETIC RADIATION
1606
APPARATUS

Fig. 16

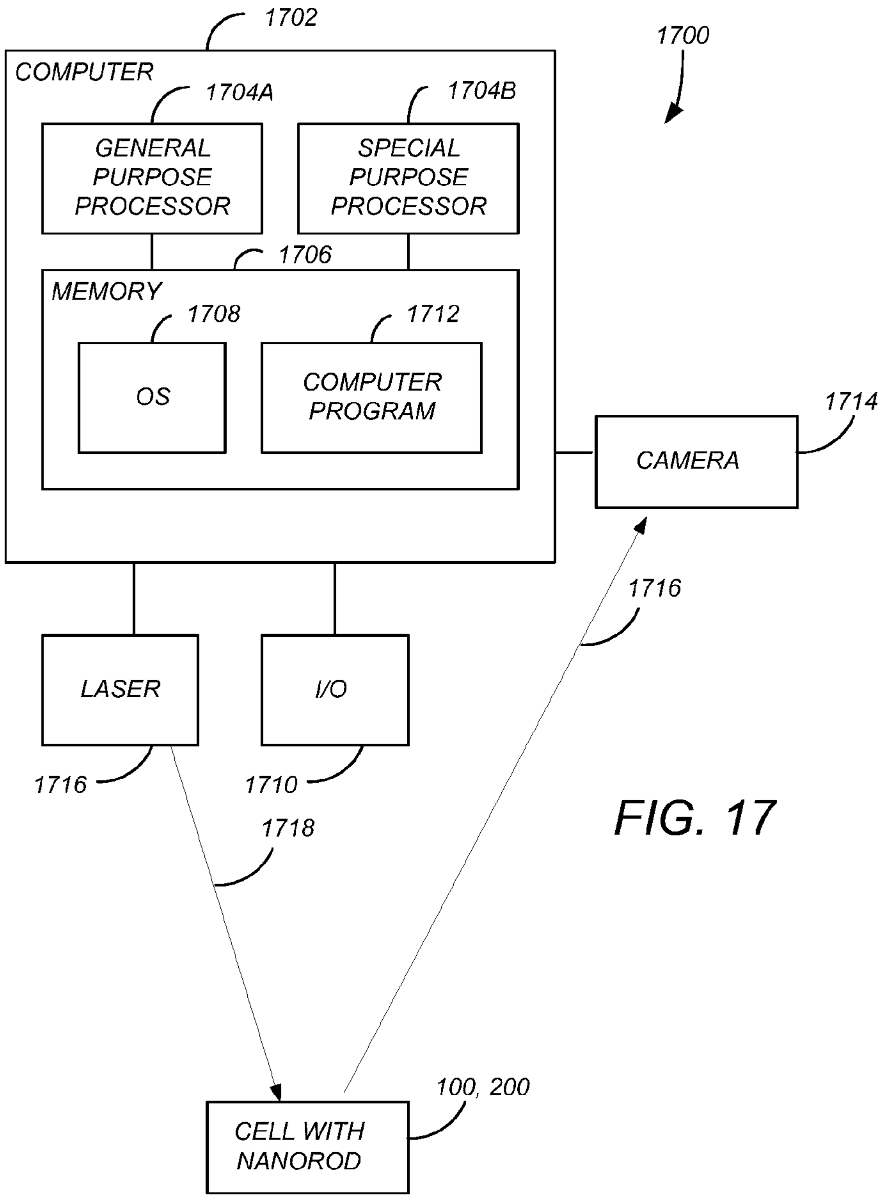
1700
1702
COMPUTER
1704A
GENERAL PURPOSE PROCESSOR
1704B
SPECIAL PURPOSE PROCESSOR
1706
MEMORY
1708
OS
1712
COMPUTER PROGRAM
1714
CAMERA
LASER
1716
I/O
1710
1718
1716
CELL WITH NANOROD
100, 200

FIG. 17

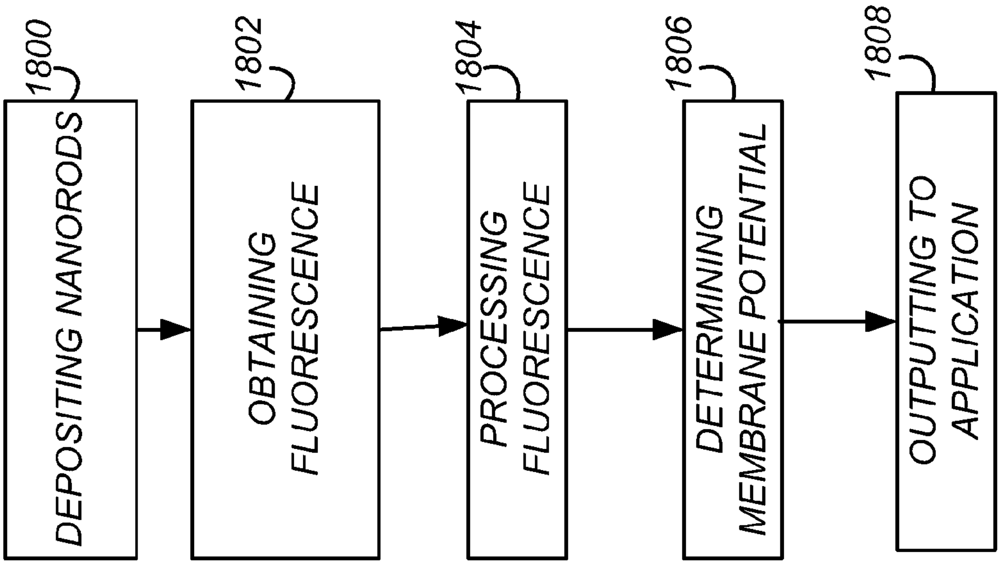
1800
DEPOSITING NANORODS
1802
OBTAINING FLUORESCENCE
1804
PROCESSING FLUORESCENCE
1806
DETERMINING MEMBRANE POTENTIAL
1808
OUTPUTTING TO APPLICATION

Fig. 18

INTERNATIONAL SEARCH REPORT

International application No.
PCT/US 18/32103

A. CLASSIFICATION OF SUBJECT MATTER
IPC(8) - G01N 33/551, G01N 33/553 (2018.01)
CPC - B82Y 15/00, G01N 33/588, Y10T 428/2991

According to International Patent Classification (IPC) or to both national classification and IPC

B. FIELDS SEARCHED

Minimum documentation searched (classification system followed by classification symbols)
See Search History Document

Documentation searched other than minimum documentation to the extent that such documents are included in the fields searched
See Search History Document

Electronic data base consulted during the international search (name of data base and, where practicable, search terms used)
See Search History Document

C. DOCUMENTS CONSIDERED TO BE RELEVANT

Category*	Citation of document, with indication, where appropriate, of the relevant passages	Relevant to claim No.
X	PARK, et al. Membrane insertion of- and membrane potential sensing by- semiconductor voltage nanosensors: feasibility demonstration, BioRxiv, 16 April 2016, pp 1-32 [online]. [Retrieved on 24 July 2018]. Retrieved from the Internet <URL: https://www.biorxiv.org/content/biorxiv/early/2016/04/16/044057.full.pdf>; Especially pg 1-8	1-4, 17
A	PINAUD, et al. Advances in fluorescence imaging with quantum dot bio-probes. Biomaterials, March 2006, Vol 27, No 9, pp 1679-1687; Abstract, pg 3	1-4, 17

☐ Further documents are listed in the continuation of Box C. ☐ See patent family annex.

* Special categories of cited documents:
"A" document defining the general state of the art which is not considered to be of particular relevance
"E" earlier application or patent but published on or after the international filing date
"L" document which may throw doubts on priority claim(s) or which is cited to establish the publication date of another citation or other special reason (as specified)
"O" document referring to an oral disclosure, use, exhibition or other means
"P" document published prior to the international filing date but later than the priority date claimed
"T" later document published after the international filing date or priority date and not in conflict with the application but cited to understand the principle or theory underlying the invention
"X" document of particular relevance; the claimed invention cannot be considered novel or cannot be considered to involve an inventive step when the document is taken alone
"Y" document of particular relevance; the claimed invention cannot be considered to involve an inventive step when the document is combined with one or more other such documents, such combination being obvious to a person skilled in the art
"&" document member of the same patent family

Date of the actual completion of the international search 23 July 2018	Date of mailing of the international search report 18 SEP 2018
Name and mailing address of the ISA/US Mail Stop PCT, Attn: ISA/US, Commissioner for Patents P.O. Box 1450, Alexandria, Virginia 22313-1450 Facsimile No. 571-273-8300	Authorized officer: Lee W. Young PCT Helpdesk: 571-272-4300 PCT OSP: 571-272-7774

INTERNATIONAL SEARCH REPORT

International application No.
PCT/US 18/32103

Box No. II Observations where certain claims were found unsearchable (Continuation of item 2 of first sheet)

This international search report has not been established in respect of certain claims under Article 17(2)(a) for the following reasons:

1. ☐ Claims Nos.:
because they relate to subject matter not required to be searched by this Authority, namely:

2. ☐ Claims Nos.:
because they relate to parts of the international application that do not comply with the prescribed requirements to such an extent that no meaningful international search can be carried out, specifically:

3. ☒ Claims Nos.: 5-16, 21-24, 29-31
because they are dependent claims and are not drafted in accordance with the second and third sentences of Rule 6.4(a).

Box No. III Observations where unity of invention is lacking (Continuation of item 3 of first sheet)

This International Searching Authority found multiple inventions in this international application, as follows:

This application contains the following inventions or groups of inventions which are not so linked as to form a single general inventive concept under PCT Rule 13.1.

Group I, claims 1-4, 17, directed to a composition comprising peptides attached to a semiconductor nanorod.

Group II, claims 18-20, 25-28, directed to an apparatus and a method for measuring a membrane potential.

*** See Supplemental Sheet to continue **

1. ☐ As all required additional search fees were timely paid by the applicant, this international search report covers all searchable claims.

2. ☐ As all searchable claims could be searched without effort justifying additional fees, this Authority did not invite payment of additional fees.

3. ☐ As only some of the required additional search fees were timely paid by the applicant, this international search report covers only those claims for which fees were paid, specifically claims Nos.:

4. ☒ No required additional search fees were timely paid by the applicant. Consequently, this international search report is restricted to the invention first mentioned in the claims; it is covered by claims Nos.:
1-4, 17

Remark on Protest

☐ The additional search fees were accompanied by the applicant's protest and, where applicable, the payment of a protest fee.

☐ The additional search fees were accompanied by the applicant's protest but the applicable protest fee was not paid within the time limit specified in the invitation.

☐ No protest accompanied the payment of additional search fees.

In Continuation of Box III. Observations where unity of invention is lacking:

The inventions listed as Groups I and II do not relate to a single special technical feature under PCT Rule 13.1 because, under PCT Rule 13.2, they lack the same or corresponding special technical features for the following reasons:

The invention of Group I does not share the special technical feature of an apparatus and a method for measuring a membrane potential required by Group II.

The inventions of Group I and II share the special technical feature of a semiconductor peptide coated nanorod. However, this shared technical feature does not represent an improvement over prior art as being anticipated by a paper titled "Peptidic ligands to control the three-dimensional self-assembly of quantum rods in aqueous media" by Bizien, et al. (Small 24 September 2014, Vol 10, No 18, pp 3707-16) (hereinafter "Bizien").

Bizien discloses a semiconductor peptide coated nanorod (pg 3, Figure 1 and its legend, peptide-QRs [core/shell quantum rods], "a) Schematic view of the whole process yielding peptide-QRs, from nanoparticles synthesis in organic solvent to ligand exchange and purification of the hydrophilic colloids. b) Chemical structure of the TCCPAC and TCCPAM peptides. c) FTIR spectra of the hydrophobic ... the TCCPAC-QRs (blue). d) 31P NMR spectra in CDCl3 of ... peptide-QRs (3)"). As the technical feature was known in the art at the time of the invention, this cannot be considered special technical feature that would otherwise unify the inventions.

Therefore, inventions of Groups I and II lack unity under PCT Rule 13 because they do not share the same or corresponding special technical feature.